nature energy

Supplementary information

https://doi.org/10.1038/s41560-026-02131-5

Quantifying the impact of cell-to-cell inconsistency on electric vehicle battery degradation and utilization

In the format provided by the authors and unedited

Supplementary Contents

Supplementary Note 1: Dataset, battery systems and data preprocessing

Dataset description

Vehicle categories. The dataset covers two EV categories: (i) five-seater passenger cars operated as ride-hailing services, and (ii) 24-seater buses used for public transportation.

Geographic distribution. As shown in Supplementary Figure 1, the 133 vehicles analyzed in this study are distributed across multiple provinces in northern, central, eastern and southern China, reflecting a broad geographic coverage and diverse operational environments. On the map, green circles mark the initial recorded locations of all vehicles on the first day of data collection, stars mark the vehicles selected for detailed analysis in the main Results. Red stars denote passenger cars with nickel-manganese-cobalt (NMC) batteries, and blue stars represent buses with lithium-iron-phosphate (LFP) batteries. Two prominent clusters of NMC passenger cars are located in Hangzhou, Zhejiang Province (eastern China) and Shenzhen, Guangdong Province (southeastern China). The primary clusters of LFP buses are situated in Xinyang, Henan Province, and Baoshan, Yunnan Province.

Temporal coverage. As shown in Supplementary Figure 2, the collection period of the entire dataset spans from June 2018 to December 2023. More than half of the vehicles have data collection periods exceeding three years. In particular, a substantial subset of vehicles was monitored continuously from February 2019 to April 2022. This long-term field coverage supports analysis across multiple calendar years and seasons.

Environmental conditions. To contextualize the operational environments, four representative deployment regions were selected: Shenzhen in Guangdong Province, Hangzhou in Zhejiang Province, Xinyang in Henan Province, and Baoshan in Yunnan Province. As shown in Supplementary Figure 3, the hourly temperature and relative humidity profiles for 2021 revealed distinct climatic regimes across these regions. Specifically, in 2021, the hourly temperature ranged from -8.0 to $36.3\,^{\circ}\mathrm{C}$, and the relative humidity from 16.3% to 100.0%. The annual average temperatures ranged from about 16.8 to $23.7\,^{\circ}\mathrm{C}$, while the annual average relative humidity varied between 73.5% and 76.7%. These variations reflect differences in latitude and proximity to the coast. The environmental data were obtained from the European Centre for Medium-Range Weather Forecasts (ECMWF).

Ambient versus pack temperature. To illustrate the relationship between ambient temperature and the internal temperature of EV battery packs, we present two representative examples in Supplementary Figure 4: an NMC passenger car operating in Shenzhen and an LFP bus operating in Baoshan. In both cases, the battery pack temperatures consistently exceed the ambient temperature, reflecting the elevated thermal environment that batteries experience during real-world operation. Despite this offset, the pack's temperature profile tracks its ambient temperature with similar temporal trends, indicating that ambient conditions exert a strong influence on pack thermal behaviour.

Battery system specifications

In this study, we investigate two representative types of power batteries commonly used in electric vehicles (EVs): NMC batteries, widely used in electric passenger cars due to their high specific energy and robust power performance; and LFP batteries, preferred in electric buses owing to their superior thermal stability and inherent safety characteristics. These two chemistries thus represent the dominant technological paradigms in the current EV landscape.

Driven by the demand for high-energy systems, the industry has increasingly favored large-format cells with higher individual capacities. This trend enables designs with fewer parallel connections and more extensive series connections. Such configurations, however, exacerbate cell-to-cell inconsistencies within battery packs. As outlined in the main text, quantifying the impact of these inconsistencies is a central aim of our study. As summarised in Supplementary Table 1, the representative NMC and LFP battery packs studied here have nominal energies of 52 kWh and 105 kWh, with nominal capacities of 150 Ah and 210 Ah, respectively. The overall voltage and capacity of each pack are determined by its internal cell configuration, denoted by an XPXS scheme (e.g., 1P95S), where the number of series-connected cells (XS) sets the pack voltage, and the number of parallel strings (XP) defines its capacity. The battery management system (BMS) maintains the terminal voltage of each cell within a specified operating range.

Key functions of the BMS

The BMS employed in both vehicle types provide a suite of core functions, including real-time monitoring, state estimation, charge and discharge regulation, thermal management, cell balancing, and coordination with vehicle-level controllers. For the 150 Ah NMC passenger cars, their BMS fulfills five principal roles:

1) Monitoring and estimation: The BMS continuously measures cell-level voltages, pack-level current, and a few temperature points in each module, while estimating the SOC and SOH. These capabilities underpin safe and efficient battery operation.

2) Charge/discharge control and protection: The system enforces charge and discharge limits and multiple protections, including overvoltage, undervoltage, overcurrent, and high- or low-temperature protection. DC fast charging is supported, with full charges typically on the order of 50 minutes and 30%–80% partial charges in about 30 minutes.

3) Thermal management: In response to sensor feedback, the BMS activates cooling or heating systems to limit temperature excursions and reduce thermal gradients across the pack.

4) Cell balancing: Passive balancing is employed to reduce voltage dispersion and slow divergence.

5) Coordination with vehicle-level controllers: The BMS communicates closely with the vehicle control unit (VCU) and motor control unit (MCU), processing signals from the charging infrastructure and vehicle sensors to ensure the safe operation of both high- and low-voltage systems.

For LFP buses, the BMS performs functions similar to those in NMC passenger cars, but its thermal management strategy reflects the distinct characteristics of LFP chemistry. LFP cells are more vulnerable to low temperatures, requiring the BMS to prioritize heat retention and mitigate efficiency losses in cold conditions, while typically demanding less intensive cooling than NMC packs. Cell-balancing strategies also differ: in the LFP buses examined here, the BMS did not incorporate explicit voltage/SOC balancing functions. Supported by a mature supply chain and stringent cell screening, an early industrial practice held that if the initial uniformity of LFP cells was tightly controlled, pack voltages could remain stable for several years without balancing. However, this approach was limited to early-generation electric buses. In current models, at least passive balancing is typically implemented, and in some cases active balancing strategies are employed.

By monitoring battery voltages, temperatures, and internal states, the BMS suppresses cell-to-cell heterogeneity, particularly in the early stages of battery life. As the pack ages and experiences thermal gradients and heterogeneous usage histories, the ability of these mechanisms to equalize cells decreases. Variability observed in later life stages therefore reflects a combination of intrinsic cell degradation and the practical limits of BMS interventions. Understanding these system-level interactions is essential for accurately attributing observed variability to underlying degradation mechanisms and operational constraints.

Data processing and selection methods

The first step in data processing and selection was to identify and remove discontinuous or interrupted data series (Supplementary Figure 5a), which could result from sensor malfunctions, communication dropouts, or storage errors. To this end, we extracted and individually examined all charging curves. Any curve identified as problematic was discarded. As a result, the final dataset consists exclusively of high-quality, continuous, and intact charging curves, regardless of their starting or ending SOC. As shown in Supplementary Figure 5e, only a small fraction (2.8%) of the original curves were affected by such issues.

The battery packs of the studied electric cars underwent both fast and slow charging. Fast charging employed constant-current (CC) or multi-stage CC protocols, with currents reaching up to 1C. As shown in Supplementary Figure 5b, the fast-charging current exhibited considerable variation across vehicles and individual events. Slow charging consisted primarily of overnight CC charging at rates around or below 0.1C, and accounted for over 40% of all charging events. A closer examination revealed that a small portion (2%) of the current data fell within the range $[0.02C, 0.09C]$ prior to reaching the 0.1C threshold, which we attribute to measurement variability. These low-current points did not exhibit the characteristic behaviour of a constant-voltage (CV) phase (for example, a sustained voltage plateau accompanied by a tapering current), and therefore were not classified as CV operation in the recorded data. Overall, most of these slow-charging curves also exhibited relatively wide SOC ranges.

Given that only field data from EV fleets were available, a low-order equivalent circuit model was employed to identify cell-level ageing indicators under operational conditions, as detailed in the Methods section of the main text. To align with the underlying assumptions of this model, we selected, as the second step of data processing, slow-charging data with wide SOC ranges—specifically, those covering 25% to 99% SOC—for estimating cell capacity and internal resistance (Supplementary Figure 5c). Note that the SOC in this real-world dataset adheres to a practical definition adopted in the field, where 100% SOC corresponds to the terminal voltage reaching the upper cutoff of 4.2 V under a C/10 current. This differs from standard laboratory protocols, in which SOC = 100% is defined by a full constant current–constant voltage (CC–CV) charge that continues until the current in the CV phase tapers to a low cutoff, such as C/30 to C/50. The laboratory definition represents an absolute full charge but is rarely achieved in real-world EV operation.

Following this data processing and selection pipeline, 10,934 charging curves from 19 NMC passenger cars were retained for model development and ageing analysis (Supplementary Figure 5e), while the LFP fleet assessment included 10 of the 17 buses (Supplementary Figure 8).

Supplementary Note 2: Extended analyses of cell inconsistency and pack-level implications

Extended analysis of pack-level implications

(1) Quantifying inconsistency and its impacts

Supporting analyses and illustrations are provided in Supplementary Figs. 6–8.

(2) Case studies of pack-level interventions

As shown in Supplementary Figure 25, we observed an instructive case in one particular EV: the vehicle accumulated a total mileage of 287,838 km, during which six of the 95 cells in its battery pack were diagnosed as faulty and subsequently replaced with new cells of the same specification. Among all cells, the healthiest cell retains an SOH of 0.93, while the most degraded cell has declined to an SOH of 0.80. The initial estimates prior to projection show even greater dispersion.

The newly replaced cells appear significantly less aged than their original counterparts, as expected, but their introduction without appropriate SOC equalization, capacity matching, or BMS recalibration inevitably increases parameter dispersion. Such an imbalance can lead to uneven current distribution during charge–discharge cycles, accelerated degradation of both the new and aged cells, and potential reductions in usable energy and pack efficiency, particularly under high-load or fast-charging conditions.

Importantly, our prognostic method captured these shifts in both capacity and resistance, and the identified changes aligned with the timing and nature of the maintenance intervention. This provides evidence that the method can detect battery state changes arising from both natural ageing and operational interventions.

In this study, one of the EV battery packs exhibited an SOH of 80.0% at the accumulated mileage of approximately 280,000 km. The battery pack comprises 95 cells, with individual cell SOH values ranging from 0.80 to 0.93, and an average SOH of 0.88 (see Supplementary Figure 26). This pack-level SOH corresponds to an overall capacity degradation of 20% and is limited by the performance of the lowest-capacity cell.

(3) Cell-to-cell variability and balancing strategies

Industrial screening and pack-assembly practices aim to minimise cell dispersion in EV battery packs. Stringent upstream and downstream quality control by battery manufacturers and vehicle OEMs helps ensure that only Grade-A cells, which meet tight limits on, for example, voltage, capacity, and internal resistance, are assembled into EV packs [1]. Consistent with these practices, our dataset shows minimal and stable cell-to-cell variability in the state of health (SOH) during early life (Supplementary Figure 27). However, variability increases markedly as the batteries age, particularly after their ageing knees. Temperature gradients associated with nonuniform cooling and cell positioning can substantially contribute to this divergence [2]. Although the vehicles in this dataset were manufactured in 2018 to 2019 and may exhibit somewhat greater initial dispersion than newer platforms, usage-induced heterogeneity in thermal exposure, state-of-charge (SOC) trajectories, and operational loading drives divergence over time, even when initial matching is tight.

Cell-to-cell differences arise from the combined effects of manufacturing variability, heterogeneous operating conditions, and progressive ageing. Cell balancing is central to mitigating the amplification of these differences. In principle, effective methods should be able to slow their propagation over time and maintain inconsistencies within a controlled range. In the NMC passenger cars studied, the BMS employs continuous passive balancing to equalize cell voltages during charging. We define the voltage spread as the difference between the maximum and minimum cell voltages in the pack, which provides a direct measure of cell-to-cell inhomogeneity. Supplementary Figure 11 shows the evolution of cell voltages and voltage spread for seven days in each of 2019, 2020, and 2021.

The voltage spread fluctuates during operation, with the largest values typically occurring during discharge, particularly toward the end of discharge. In contrast, once charging begins, the spread is quickly reduced thanks to cell equalization and the fact that cells sequentially enter the voltage plateau region (highlighted in the inset of Supplementary Figure 11c). Although the spread increases again mid-charge, it declines to a stable level near full charge, reflecting the effect of passive balancing. This strategy effectively suppresses long-term divergence: the voltage spread remains within approximately 50 mV by 2020 and rarely exceeds 100 mV even at later ageing stages in 2021. These results indicate that continuous passive balancing helps stabilize pack behaviour and mitigates voltage heterogeneity despite progressive ageing.

To further examine this phenomenon in the representative passenger car, we analyzed all cell voltage data collected under constant-current slow-charging conditions to compute the voltage spread. The results are presented in Supplementary Figure 12. Consistent with Supplementary Figure 11, the voltage spread increases during discharge and typically peaks near the end of deep discharge, with this trend intensifying with ageing. Once charging begins, the spread decreases, and over successive cycles long-term passive balancing maintains the spread at a low and stable level during charge.

By contrast, the LFP buses do not incorporate explicit balancing functions in their BMS. Supplementary Figure 13a–d shows the evolution of cell voltages and the voltage spread over seven consecutive days in each of 2019, 2020, 2021, and 2022, respectively. As in the NMC passenger cars, the voltage spread fluctuates during operation; however, the largest values typically occur at the end of charge. This behaviour is characteristic of LFP batteries, which exhibit an extended and nearly flat voltage plateau across most of the usable SOC range. Within this plateau, even cells with substantial inhomogeneity display nearly identical terminal voltages, as evident in Supplementary Figures 13–14. Beyond the plateau, as end of charge is approached, cell voltages rise steeply, so small SOC differences translate into large voltage deviations. In addition, the apparent persistence of high voltage-spread values after charge completion (visible as many parallel red lines in Supplementary Figure 13) reflects the absence of measurements during idle periods, with the plotted straight lines simply connecting data gaps.

In this LFP battery pack, cell-to-cell voltage inconsistency increases with ageing. In the early years of operation, the voltage spread is limited to about 100 mV (Supplementary Figure 13a–b), whereas in later stages it exceeds 200 mV (Supplementary Figure 13d) and can reach 300 mV (Supplementary Figure 14), which is consistent with the lack of balancing interventions. The comparison between the two vehicle types indicates that system-level control strategies, together with intrinsic ageing mechanisms, strongly influence the evolution of variability.

Distinguishing automotive-grade and research-grade cells

Many previous studies on cell heterogeneity and pack-level behaviour have relied on research-grade or commercially available cells that are not necessarily automotive-grade. Such cells, often representing surplus from industrial screening processes, may exhibit broader variability in electrochemical properties due to relaxed quality control standards. Consequently, the variability observed in those studies may not accurately reflect the tighter tolerances characteristic of real EV battery packs.

In contrast, this study leverages large-scale, real-world data from EVs in operation, where all cells have undergone stringent screening by both cell manufacturers and original equipment manufacturers (OEMs). Only cells meeting strict criteria—such as tight distributions in capacity, voltage, and internal resistance—are selected for integration into automotive battery packs. This ensures high initial uniformity and safety, aligning with the quality requirements of automotive-grade systems.

Our analysis confirms this expectation: during the early stages of battery life, cell-to-cell variability in SOH is minimal. However, as ageing progresses, particularly beyond a critical degradation threshold, this variability increases substantially. This rise reflects not only the emergence of intrinsic degradation mechanisms, but also the limited ability of the current BMS to fully equalize cell performance under non-uniform stress conditions.

Balancing and reconfiguration in battery systems

Cell balancing is essential for maintaining uniform SOC and voltage among cells, and is typically realized through either passive or active approaches [3]. Passive balancing dissipates excess energy from higher-voltage cells as heat via resistors. Although simple and low-cost, it is inherently inefficient and suitable only for small packs because of increased heat generation and the associated cooling demand [4]. In contrast, active balancing redistributes charge from higher-SOC cells to lower-SOC ones, thereby conserving energy within the pack and reducing SOC disparities. By improving uniformity, active balancing enhances both pack performance and lifetime [5, 6].

Regardless of the balancing method, conventional battery packs with fixed configurations cannot bypass faulty cells or adapt to non-uniform cell degradation. To overcome this limitation, reconfigurable battery systems (RBSs) have emerged as a promising architectural solution to mitigate inconsistency. By integrating controllable power electronics around cells, modules, or subpacks, an RBS can dynamically alter its electrical topology, engaging or bypassing individual units during operation [7, 8, 9]. This flexibility enables adaptive utilisation of battery units according to their real-time states and represents a new paradigm in battery management. Potential benefits include enhanced reliability, improved SOC and thermal uniformity, extended lifetime, and the coordination of batteries of varying chemistries. These advantages, however, come with practical challenges. The inclusion of reconfiguration circuits and communication interfaces increases hardware complexity, parasitic losses, and cost. Frequent topology changes require reliable protection schemes and fast control coordination, while the expanded configuration space demands efficient optimisation algorithms. Future development must therefore balance these trade-offs, quantitatively assessing how gains in lifetime, safety, and energy utilisation offset the added system overhead.

The mitigation strategies of battery inconsistency discussed above offer distinct advantages, limitations, and domains of suitability. Importantly, the proposed metrics and their fleet-derived values in this study provide quantitative guidance for determining when and how balancing or reconfiguration strategies should be deployed in EV battery systems in practice.

Supplementary Note 3: Parameter identification and neural-network normalisation

Details of Step 1 and Step 2

OCV reconstruction. Accurate identification of cell-level ageing indicators requires a consistent OCV–SOC relationship. As illustrated in Supplementary Figure 15, wide-range, low-rate constant-current (CC) charging processes are first extracted to record terminal voltage V and charging current I. The ohmic resistance R_0 is independently anchored from current step transitions as described in the main text. The open-circuit voltage is then computed as

$$\mathrm{OCV} = V - IR_0. \tag{1}$$

The green segment in Supplementary Figure 15 represents the directly obtained partial OCV–SOC profile. Extrapolation is performed at both ends of the SOC range using transitional anchor points: the low-SOC region is fitted with a fourth-degree polynomial and the high-SOC region with a linear function. Finally, a tenth-degree polynomial is used to reconstruct a smooth OCV–SOC curve across the entire SOC range.

Excitation selection and dimensionality reduction. A first-order ECM with parameters $\{R_0, R_p, C_p, C, V_{p,0}, \mathrm{SOC}_0\}$ is, in general, not globally structurally identifiable if all parameters and initial conditions are treated as free variables under arbitrary excitation. In the proposed framework, two constraints are imposed. First, R_0 is independently anchored prior to optimisation. Second, parameter identification is restricted to quasi-steady segments of slow CC charging, sufficiently long after charging initiation such that the transient polarization dynamics have effectively converged.

Under constant current $I(t) = I$, the polarization voltage satisfies

$$V_p(t) = R_p I + \left(V_{p,0} - R_p I\right)\exp\left(-\frac{t}{R_p C_p}\right). \tag{2}$$

For the selected charging windows where $t \gg R_p C_p$, the exponential term becomes negligible and

$$V_p(t) \approx R_p I. \tag{3}$$

Although the polarization time constant $\tau = R_p C_p$ may vary and can increase with battery ageing, this does not invalidate the quasi-steady approximation under the selected excitation regime. The charging segments used for identification are slow constant-current events with durations on the order of hours, whereas the polarization relaxation processes represented by a first-order RC branch occur over much shorter time scales. Moreover, the selected identification windows are taken sufficiently long after charging initiation, so any residual transient term $(V_{p,0} - R_p I)\exp(-t/R_p C_p)$ has effectively decayed before parameter fitting. Therefore, even if τ increases during ageing, the condition $t \gg R_p C_p$ remains satisfied for the analyzed charging windows, and C_p and $V_{p,0}$ do not enter the reduced quasi-steady estimation problem as independent decision variables.

The terminal voltage therefore reduces to

$$V(t) \approx \mathrm{OCV}(\mathrm{SOC}(t)) + R_p I + R_0 I. \tag{4}$$

In this regime, C_p and $V_{p,0}$ no longer appear as independent decision variables, and the effective free parameter set reduces to $\{R_p, C, \mathrm{SOC}_0\}$.

Local identifiability. Within the selected SOC window, the remaining parameters influence the voltage trajectory in qualitatively distinct directions. The parameter R_p introduces an approximately constant vertical offset, SOC_0 shifts the initial position along the OCV–SOC curve, and C governs the time scaling of SOC evolution under constant current. The reduced parameter set is fitted over long constant-current segments with sufficient data samples, providing adequate information for estimation. Provided that the OCV–SOC relation is monotonic and sufficiently nonlinear in the identification window, these influence directions are locally separable, ensuring local identifiability of the reduced parameter set under the selected slow CC, quasi-steady excitation conditions.

Assumptions underlying the temperature normalisation

Within Step 3 of the proposed framework, the temperature normalisation assumes that the influence of temperature dynamics on the estimated capacity and internal resistance can be represented through their long-term statistical properties rather than through instantaneous temperature fluctuations. In practical vehicle operation, temperature varies continuously due to environmental conditions, driving load, and thermal management. These variations may introduce both reversible and irreversible effects on battery behaviour. However, when aggregated over operational windows such as charging events, their cumulative influence on battery ageing is reflected in the statistical properties of the operating conditions experienced by the battery.

Because the neural-network models are trained on multi-year fleet data spanning multiple seasons and a wide range of temperatures, the training data provide diverse operational conditions from which the models can learn empirical relationships between the ageing indicators and the associated operational factors. This enables the identified capacity and resistance values to be projected to a common reference condition for consistent comparison.

Neural network architecture and training strategy

The neural network used in this study is a supervised feedforward fully connected neural network (FCNN). The influencing factors were used as input features, while the real-time estimated resistance or capacity served as output targets. The choice of an FCNN is motivated by its strong ability to capture nonlinear and coupled relationships between operating conditions and battery parameters.

Neural network architecture. The network consists of a single hidden layer comprising 16 neurons, which provides a good balance between model expressiveness and the risk of overfitting. The rectified linear unit (ReLU) activation function was adopted in the hidden layer to capture nonlinear dependencies, while a linear activation was used in the output layer to predict continuous variables (resistance or capacity). To improve generalization, a dropout layer with a dropout rate of 0.1 was applied after the hidden layer. The model was trained using the Adam optimiser with a learning rate of 0.001 and a mean-squared-error (MSE) loss function, which directly quantifies the deviation between predictions and reference values. Early stopping was implemented with a patience of 20 epochs, terminating training once the validation loss ceased to improve.

Training and validation. The dataset was randomly partitioned into training (70%), validation (15%), and testing (15%) subsets. Each model was trained for up to 300 epochs, and the weights corresponding to the minimum validation loss were retained for subsequent evaluation.

Mathematical representation. For predicting the internal resistance R_0, the NN model is expressed as:

$$R_0(k) = f_R(I(k), V(k), SOC(k), T_{\mathrm{avg}}(k), T_{\mathrm{amb}}(k), d(k)), \tag{5}$$

where $T_{\mathrm{avg}}(k)$ and $T_{\mathrm{amb}}(k)$ denote the pack-average and ambient temperatures, respectively, and $d(k)$ represents the accumulated driving distance. The output $R_0(k)$ corresponds to the internal resistance identified in Step 2 of the proposed method, as described in the Methods section of the manuscript.

For capacity prediction, the NN model is formulated as

$$C(n) = f_C(I_{\mathrm{avg}}(n), T_{\mathrm{avgc}}(n), T_{\mathrm{ambc}}(n), d(n)), \tag{6}$$

where $I_{\mathrm{avg}}(n)$ is the average current during the n-th charging cycle, $T_{\mathrm{avgc}}(n)$ and $T_{\mathrm{ambc}}(n)$ are the average pack and ambient temperatures, and $d(n)$ is the average accumulated driving distance.

Model application and evaluation. After training, the NN models f_R and f_C can be applied under arbitrary operational conditions by providing the corresponding input values. For fleet-level assessment, reference resistance and capacity at specified mileage intervals are computed as:

$$R_0(m) = f_R\left(\overline{I}, \overline{V}, \overline{SOC}, \overline{T}_{\mathrm{avg}}, \overline{T}_{\mathrm{amb}}, d(m)\right), \tag{7}$$

$$C(m) = f_C\left(\overline{I}_{\mathrm{avg}}, \overline{T}_{\mathrm{avgc}}, \overline{T}_{\mathrm{ambc}}, d(m)\right), \tag{8}$$

where overlined variables denote the mean of input features across a specified driving or charging window, and m is the evaluation mileage.

Supplementary Note 4: Validation and fleet-level robustness analyses

Validation of the proposed framework

In real-world EV fleets, ground truth for cell-level capacity and resistance evolution is generally unavailable because the batteries remain in active service and cannot be periodically characterised under controlled laboratory conditions. Consequently, direct verification of the estimated ageing trajectories against complete reference trajectories is not feasible for fleet-operated batteries.

To address this limitation, the proposed framework is assessed through complementary analyses using operational fleet data, beginning-of-life (BoL) reference measurements from an independent EV fleet, and controlled laboratory datasets with known reference measurements. The fleet-based analyses comprise a comparison with BoL measurements obtained under controlled temperature and SOC conditions and a sensitivity analysis using the NMC passenger-car fleet dataset analysed in this study, in which controlled BMS measurement perturbations are superimposed on the original signals. The laboratory datasets are used to assess key components of the estimation pipeline, including reconstruction of the OCV–SOC relationship and identification of capacity and resistance across different ageing states.

(1) Validation using fleet operational data

(a1) Validation against BoL measurements. We further assessed the proposed method using BoL measurements from batteries installed in an independent EV fleet [10]. Measurements were obtained under different temperature and SOC conditions, providing BoL reference data. Using the proposed method, we estimated the dependence of pack resistance on temperature and SOC (see Supplementary Figure 16). The neural-network estimates agree closely with the experimental BoL measurements (green crosses), particularly in regions with dense training data. The estimated resistance decreases monotonically with increasing temperature, consistent with the expected Arrhenius-type temperature dependence. The neural-network model also reproduces the observed parabolic dependence of internal resistance on SOC.

(b1) Robustness under BMS measurement perturbations. To evaluate the sensitivity of the proposed parameter identification framework to BMS measurement perturbations, we used a subset of cells from the NMC passenger-car fleet dataset analysed in this study. Representative charging events were extracted for analysis. The baseline signals were routinely recorded by in-vehicle BMSs during real-world operation and therefore retain the sensing and communication characteristics of the fleet data. Controlled perturbations were then superimposed on these original measurements to assess the effect of additional sensing errors on the parameter-identification results.

Specifically, four representative categories of sensing disturbances were considered: additive Gaussian voltage noise (σ = 2 mV), sparse sampling (retaining one in every five samples), systematic voltage bias (±5 mV), and synchronization errors introduced as temporal misalignment between voltage and current signals. A representative segment of the resulting perturbed voltage trajectories is shown in Supplementary Figure 17.

For each disturbance scenario, the apparent cell capacity was re-estimated using the parameter identification procedure described in Step 2 of the proposed framework. The baseline reference corresponds to the identification result obtained from the original fleet measurements without introducing additional perturbations. To evaluate statistical variability, 100 Monte Carlo identification trials were performed for each disturbance scenario.

The resulting distributions of normalised capacity estimates are summarised in Supplementary Figure 18 for three representative mileage levels (82,519 km, 238,390 km, and 268,964 km) of an EV in the fleet dataset. Across all disturbance scenarios, the median estimates remain closely aligned with the baseline identification results, indicating that the parameter identification procedure introduces little systematic bias even under significant sensing perturbations. For sparse sampling, systematic bias, and synchronization error, the estimated capacities are tightly concentrated around the baseline and largely remain within the ±1% deviation band across the three mileage levels, spanning a wide range of battery ageing states. By contrast, Gaussian noise produces a broader spread, with part of the distribution extending beyond this band. Importantly, these perturbation-induced deviations are still substantially smaller than the cell-to-cell capacity variations observed in the fleet dataset, particularly by the end of life (see Fig. 3**g** in the main text). This separation of scales indicates that typical BMS sensing imperfections have limited influence on the calculated cell inconsistencies.

(c1) Stability of neural-network training. Owing to the inherent stochasticity of the training process and the intrinsic characteristics of NN algorithms, model performance may vary, particularly when the models are used to infer functional relationships in data-sparse regions or beyond the range well represented in the training dataset. To quantitatively assess the stability and robustness of neural-network training, we retrained the capacity and resistance models 100 times with different random seeds using the NMC passenger-car fleet dataset analysed in this study. The predictions from all runs were used to calculate the mean trajectories and the 5–95% confidence intervals. For illustration, we selected one battery cell from the dataset and applied the trained models to estimate its capacity and resistance under both operational conditions and a standardised reference condition.

Supplementary Figure 19 presents the estimated SOH and resistance trajectories of the selected cell under standardised conditions across the 100 independently trained models. The results show that both trajectories remain highly consistent across different training runs, as indicated by the narrow 5–95% confidence intervals over most of the mileage range. The confidence intervals become wider at very high mileages, particularly above 300,000 km, reflecting the reduced availability of training samples in this region and the resulting increase in extrapolation uncertainty. Overall, the repeated-training analysis demonstrates that the proposed method provides stable and reproducible estimates despite the stochastic nature of neural-network training.

(2) Validation using laboratory datasets

(a2) Parameter identification under dynamic operating profiles. The accuracy and robustness of the parameter identification method introduced in the Methods section (Step 2) were evaluated using a hybrid pulse power characterisation (HPPC) profile, which subjects the cell to repeated charge–discharge current pulses and is widely used to validate ECM-based dynamic voltage predictions. Supplementary Figure 20a compares the measured voltage with the model-predicted response obtained using the identified parameters. Across a set of transient current steps (Supplementary Figure 20b), the fitted voltage closely follows the measured trajectory, with errors remaining tightly bounded throughout the full HPPC sequence. The resulting root-mean-square error (RMSE) is 4.6 mV, indicating that the identified parameters capture the cell's dynamic voltage behaviour with high fidelity. This level of accuracy provides a reliable foundation for the implementation of Step 3 in the overall approach, as well as for the subsequent analyses.

(b2) Validation of the OCV–SOC curve. To evaluate the accuracy of the OCV–SOC curve extracted by the method described in the Methods section of the main text, we used publicly available degradation data from the Oxford Battery Degradation Dataset 1 [11, 12]. This dataset contains measurements from eight Kokam lithium-ion pouch cells tested under controlled laboratory conditions. All cells were cycled in a thermal chamber at 40°C using a 1C constant current–constant voltage (CCCV) charging protocol, followed by discharging under an urban Artemis drive-cycle profile. Reference performance tests, including low-current OCV measurements at 40 mA, were conducted every 100 cycles to characterise cell behaviour across different ageing levels. As a representative example, the 3,000th cycle of "Cell1" was selected to evaluate the accuracy of the reconstructed OCV–SOC relationship. The OCV identification

conditions described in the Methods were applied during the evaluation.

The results are shown in Supplementary Figure 21. The mean absolute relative error (MARE) is 0.19%, and the root-mean-square error (RMSE) is 0.015. Although the error increases at very low SOC, real-world EV operation rarely occupies this region. For SOC > 5 %, the error rapidly decreases to an MARE of 0.11%. These results demonstrate that the reconstructed OCV–SOC curve is highly accurate over the practical operating range and provides a reliable basis for the subsequent parameter identification and normalisation steps (Steps 2–3) of the proposed framework.

(c2) Parameter identification across varying SOH. Using the same Oxford Battery Degradation Dataset described above, we further evaluated the accuracy of the proposed parameter identification method across different ageing levels. Specifically, the test battery with ID "Cell1" was selected to assess the estimation accuracy of capacity-defined SOH and internal resistance. As presented in Supplementary Figure 22, the estimated values closely match the ground-truth measurements across the ageing trajectory. Quantitatively, the proposed method achieved an MARE of 0.71% for the capacity-defined SOH and 0.89% for internal resistance. These results confirm the effectiveness and reliability of our estimation approach over a wide range of battery ageing states.

Fleet-level statistical characteristics of operating stress

The statistical distributions of temperature, SOC, depth of discharge (DOD), charging current, and driving current for the studied datasets are shown in Supplementary Figures 23–24. These distributions provide insights into real-world battery operation. For example, the SOC and DOD distributions delineate the operational window of the batteries, while charging/driving current and temperature distributions reveal the dynamic load profiles and thermal environments encountered in field use.

Supplementary Table 1

Supplementary Table 1 | Specifications of the studied electric vehicle batteries

Parameters	Electric passenger cars	Electric buses
Nominal pack energy	52 kWh	105 kWh
Nominal pack capacity	150 Ah	210 Ah
Cathode	NMC	LFP
Anode	Graphite	Graphite
Pack configuration	1P95S	1P156S
Upper limit of cell voltage	4.25 V	3.65 V
Lower limit of cell voltage	2.8 V	2.5 V

Supplementary Figure 1

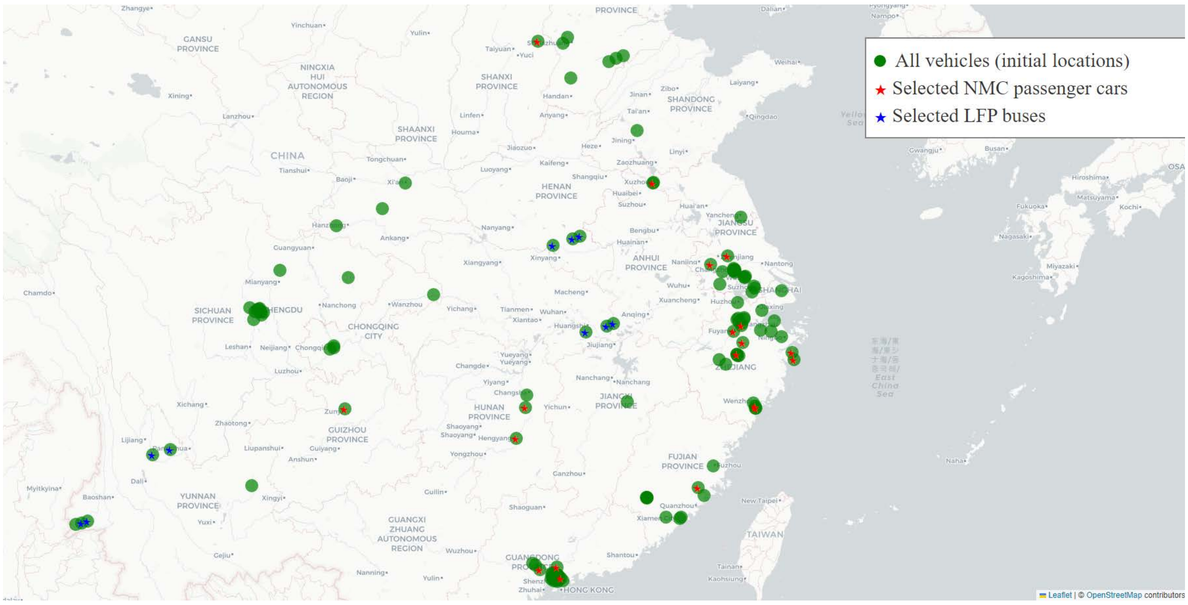

Supplementary Figure 1 | Geographic distribution of vehicle locations. The mapped locations extend from Beijing to Shenzhen, and from Baoshan to Shanghai and Ningbo, approximately 22.5–39.9°N and 99.2–121.6°E, indicating a wide range of operational environments. Green circles mark initial recorded locations on the first data-collection day; stars indicate vehicles selected for detailed analysis in the Results. Red stars are NMC passenger cars; blue stars are LFP buses.

Supplementary Figure 2

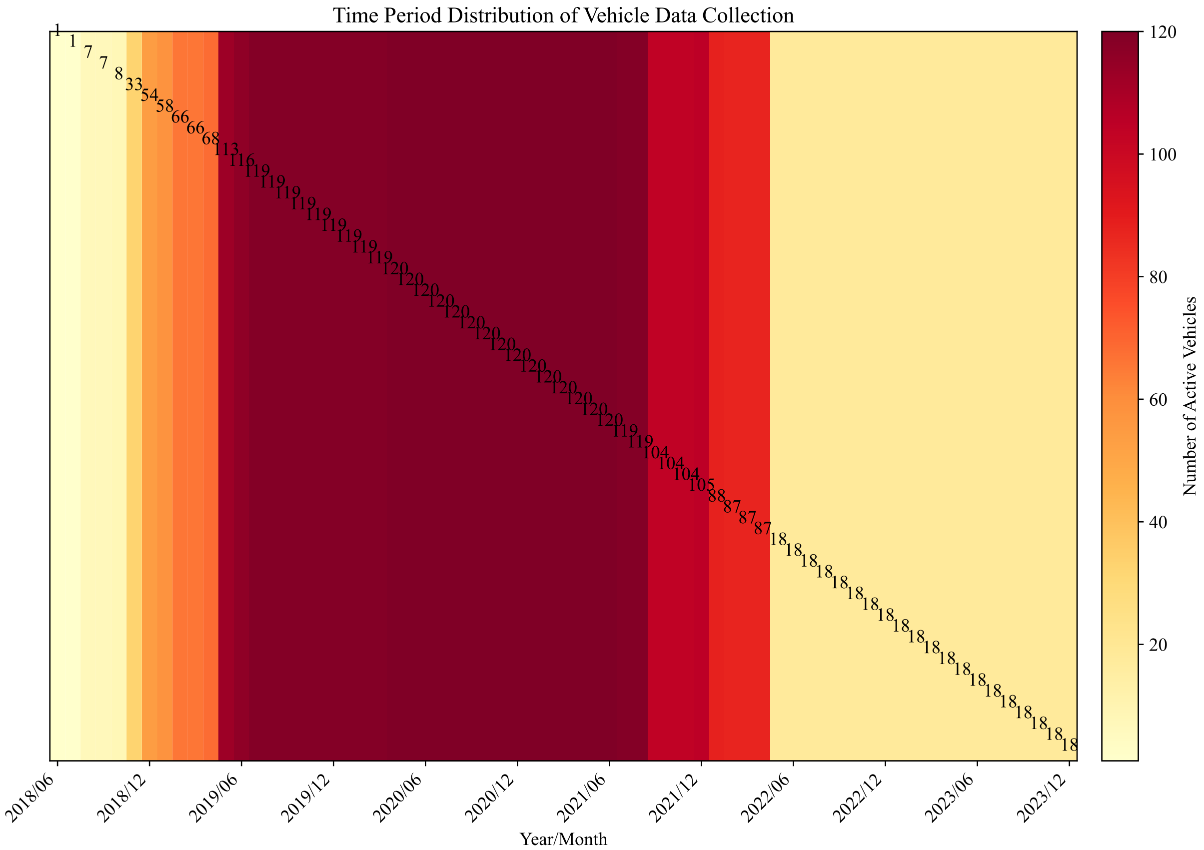

Supplementary Figure 2 | Time period distribution of vehicle data collection. Heat map of the number of active vehicles contributing data by month from mid-2018 to end-2023. Darker colors indicate more active vehicles.

Supplementary Figure 3

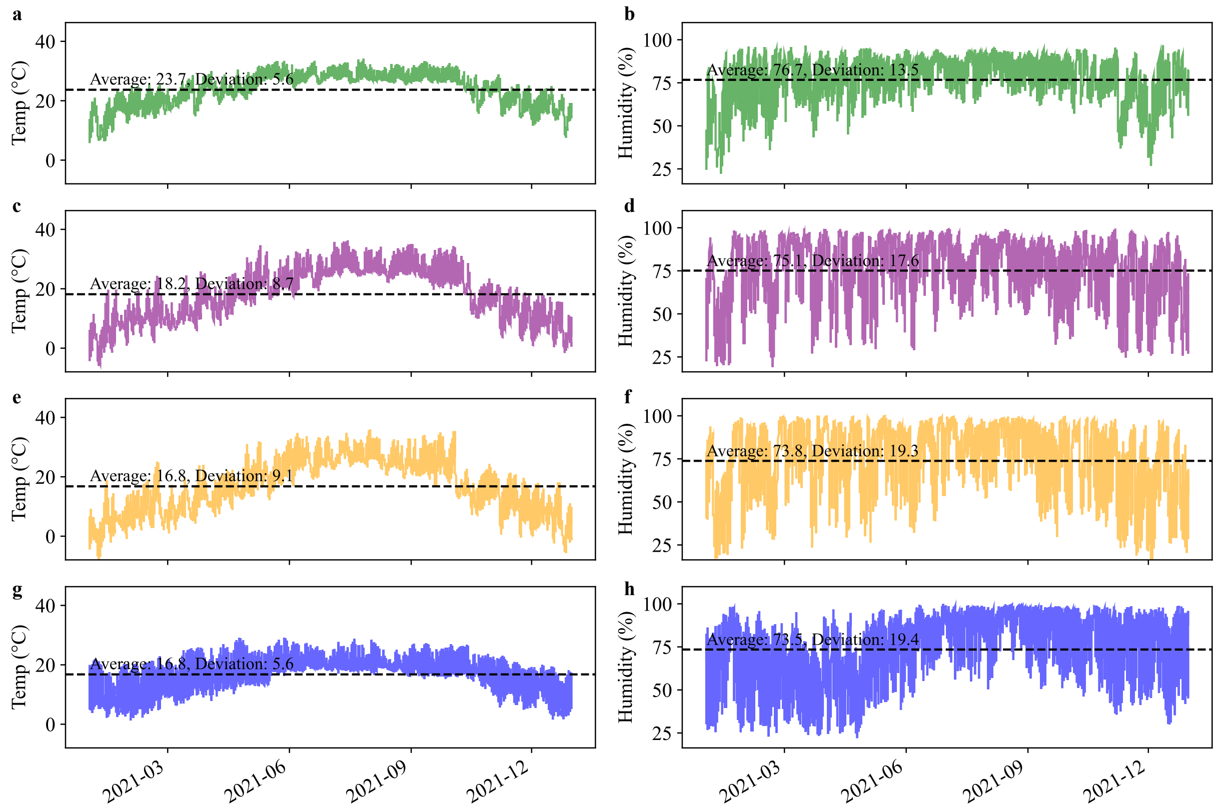

Supplementary Figure 3 | Environmental conditions across four representative vehicle deployment regions in 2021. Hourly temperature and relative humidity profiles in Shenzhen in Guangdong Province (**a, b**), Hangzhou in Zhejiang Province (**c, d**), Xinyang in Henan Province (**e, f**), and Baoshan in Yunnan Province (**g, h**). Dashed lines indicate the annual mean values for each region, with accompanying standard deviations. Source: ECMWF.

Supplementary Figure 4

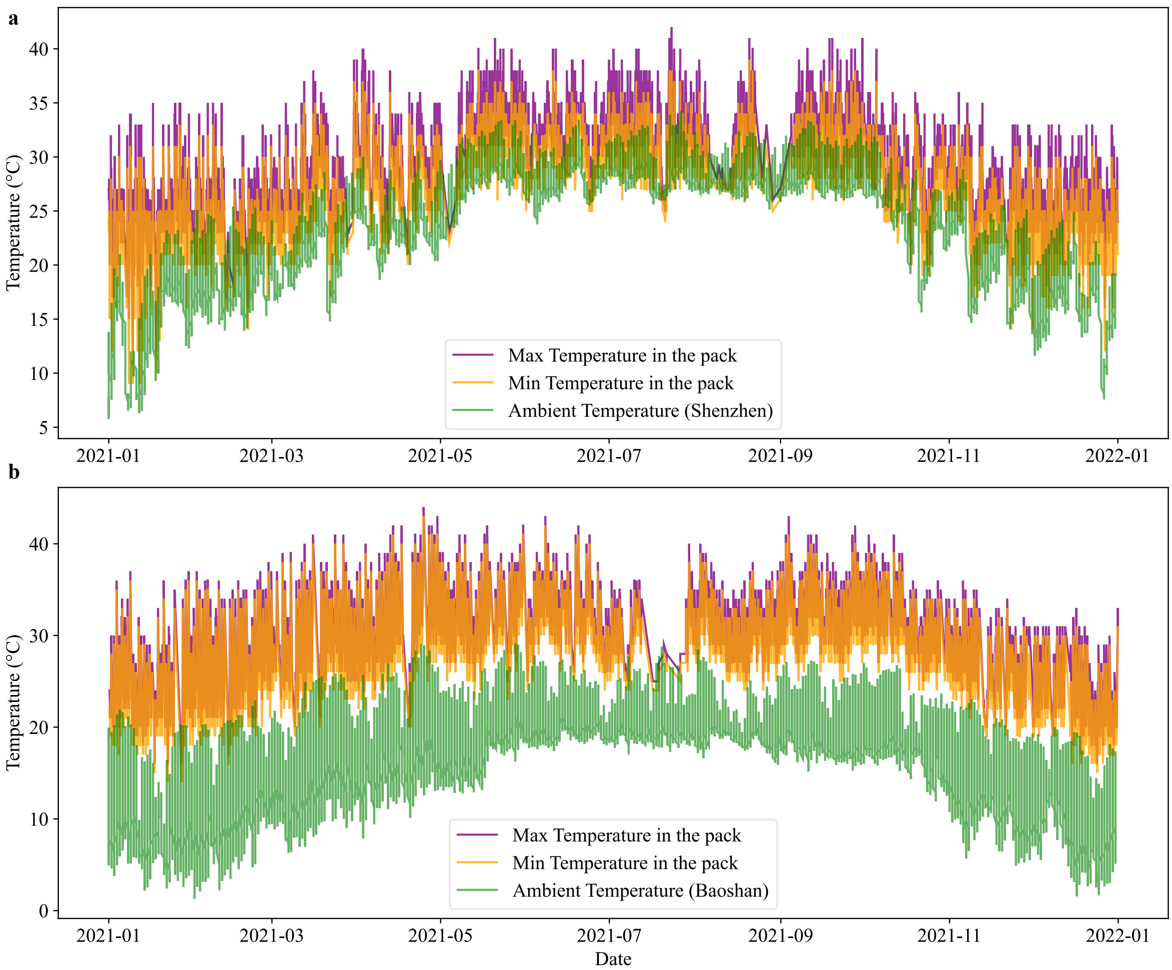

Supplementary Figure 4 | Comparison of ambient and battery-pack temperatures under real-world conditions. Ambient temperature is plotted together with the profiles of the instantaneous maximum and minimum temperatures reported by the pack's temperature sensors for two representative vehicles in 2021. These curves are sensor-derived envelopes over time and may not coincide with the absolute pack extremes. **a**, An NMC passenger car operating in Shenzhen. **b**, An LFP bus operating in Baoshan.

Supplementary Figure 5

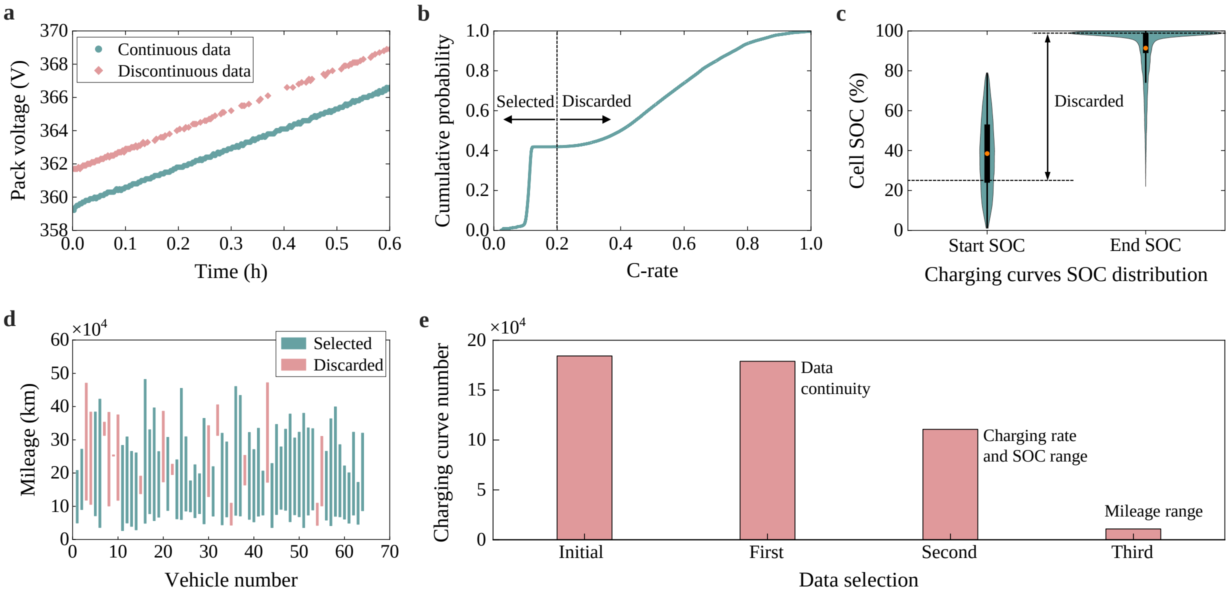

Supplementary Figure 5 | The three-step data selection process for real-world vehicle operation data, exemplified by electric cars with NMC batteries. a, The initial selection step retains continuous data and removes discontinuous data. **b**, The first part of the secondary selection step retains low-rate charging curves with current rates below 0.2C. **c**, The second part of the secondary selection step selects charging curves that cover an SOC range from 25% to 99%, excluding those starting above 25% SOC or ending below 99% SOC. **d**, The exemplified third selection step excludes vehicles with initial mileages exceeding 100,000 kilometers and those with insufficient mileage (e.g., vehicles 35 and 54). **e**, The progression of the number of charging curves retained at each step of the data selection process.

Supplementary Figure 6

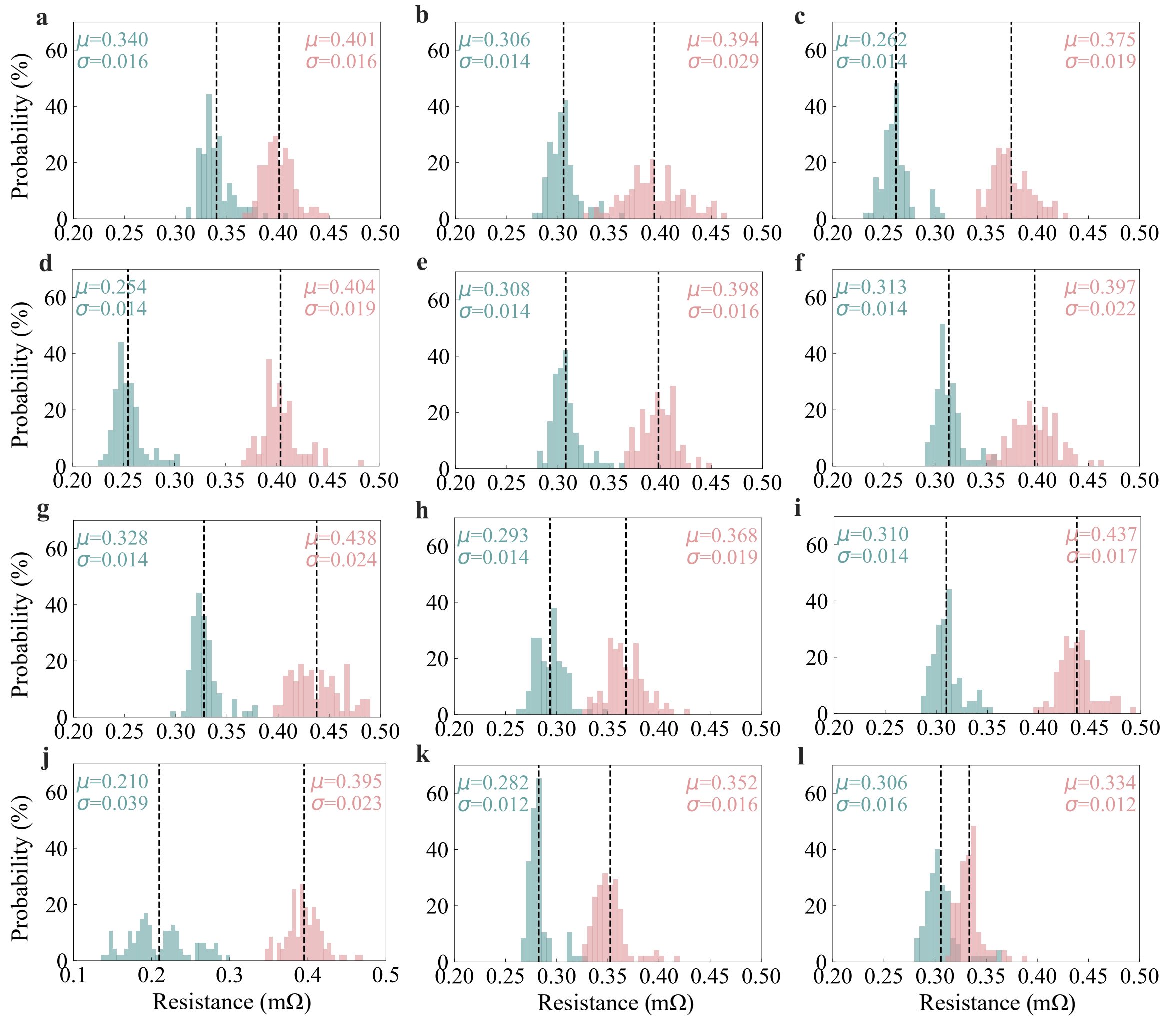

Supplementary Figure 6 | Frequency histograms of normalised resistance distributions at early (80,000 km, 27 °C; blue) and late (280,000 km, 27 °C; pink) stages of battery life for 12 passenger cars equipped with NMC batteries. Each panel (**a**–**l**) corresponds to a different vehicle, showing the mean (μ) and standard deviation (σ) values for the resistance distributions. Vertical dashed lines indicate mean resistance values, illustrating the ageing progression from early to late life stages.

Supplementary Figure 7

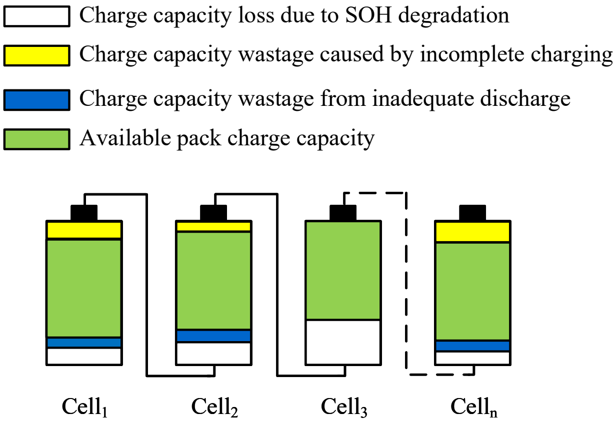

Supplementary Figure 7 | Illustration of cell-to-cell inconsistency concerning charge capacity and associated losses in a battery pack with all cells connected in series. The diagram shows variations in charge capacity utilisation among individual cells, highlighting different forms of loss: the white region represents charge capacity loss due to SOH degradation; the yellow and blue regions indicate charge capacity wastage from incomplete charging and inadequate discharge, respectively; and the green region represents the available pack charge capacity, which is limited by the most degraded cell. This inconsistency reduces the overall usable charge capacity and energy of the battery pack.

Supplementary Figure 8

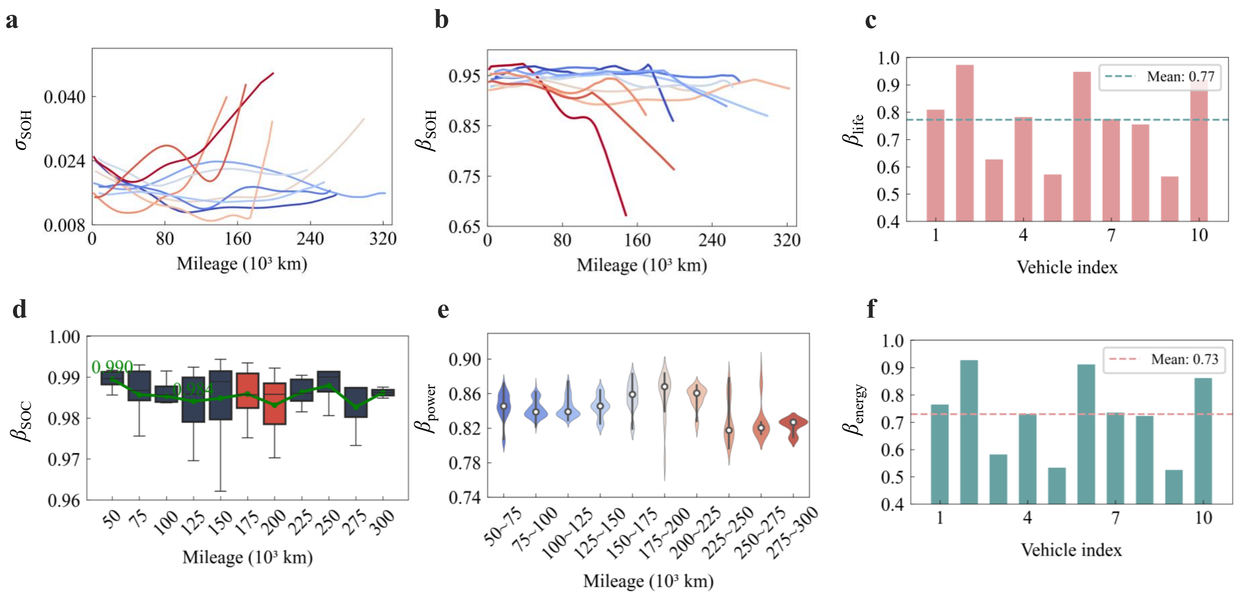

Supplementary Figure 8 | Impact of cell inconsistency on six performance metrics in LFP battery systems for electric buses. a, Standard deviation of cell SOH values within a pack (σ_{SOH}), plotted against accumulated mileage for each bus. **b**, SOH utilisation rate in each vehicle (β_{SOH}), dominated by the most aged cell. At the end of life (EOL), the fleet-average $\beta_{\mathrm{SOH}}$is 0.925, corresponding to a 7.5% reduction in SOH due to cell dispersion. **c**, utilisation rate of battery lifetime (β_{life}), showing the extent of lifetime reduction due to early retirement of the most aged cell. The fleet-average β_{life} is 0.772. **d**, utilisation rate of battery SOC (β_{SOC}), which quantifies the impact of cell inconsistency on the pack's actual charged capacity. Red box plots mark stages of pronounced decline. Before 125,000 km, the fleet-average β_{SOC} declines with mileage, reflecting increasing SOC imbalance. Note that β_{SOC} values are clearly lower than those for electric cars shown in Fig. 5 of the main text, reflecting differences in their voltage balancing strategies. This is consistent with the analysis of the results in Supplementary Figures 11–14. Beyond 125,000 km, as fewer buses reach the same mileage, the average β_{SOC} no longer evolves monotonically. **e**, utilisation rate of battery power capability (β_{power}), limited by cell resistance inconsistencies. The fleet- and mileage-averaged β_{power} is 0.849. **f**, utilisation rate of battery energy resources (β_{energy}), determined by β_{SOC} and β_{life}. The fleet-average β_{energy} is 0.73. For the box plots in **d**, the centre line indicates the median, box bounds indicate the 25th and 75th percentiles, and whiskers extend to the most extreme non-outlier values within 1.5 times the interquartile range; outliers are not shown. For the violin plots in **e**, the width represents the distribution density of values within each mileage bin.

Supplementary Figure 9

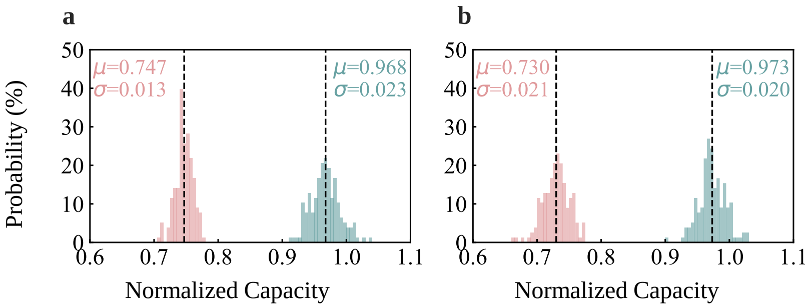

Supplementary Figure 9 | Frequency histograms of normalised capacity distributions at early (80,000 km, 32 °C; blue) and late life stages (190,000 km, 32 °C; pink) for two electric buses equipped with LFP batteries. Panels **a** and **b** depict normalised capacity distributions at early (blue) and late (pink) stages of battery ageing. Dashed vertical lines indicate mean values, demonstrating a clear shift toward lower capacity at later stages, indicative of progressive battery degradation. The means (μ) and standard deviations (σ) for each stage are annotated, highlighting the marked decline in battery health over time.

Supplementary Figure 10

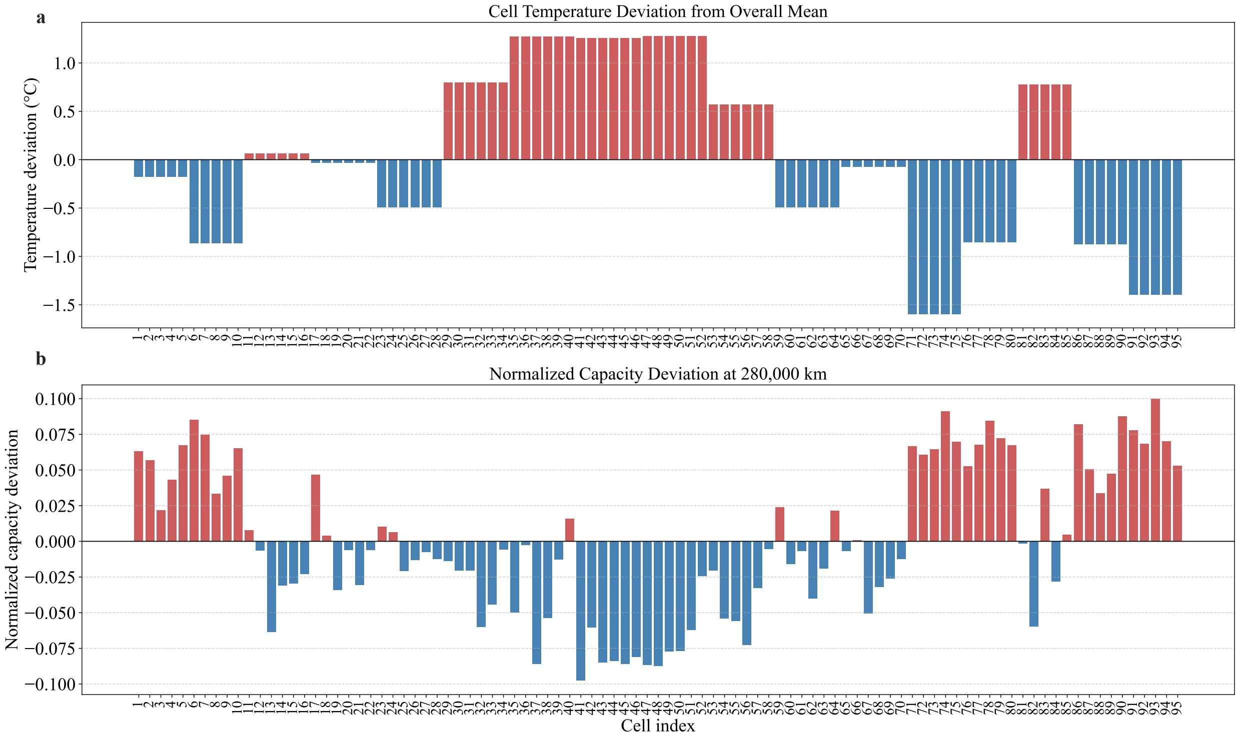

Supplementary Figure 10 | Correlation between historical average cell temperature and cell-level SOH deviations in an NMC battery pack after 280,000 km. a, Deviations of individual cell temperatures from the pack's average historical temperature. Positive (red) and negative (blue) deviations indicate cells historically operating at higher or lower temperatures, respectively. **b**, Corresponding deviations in SOH for each cell, demonstrating that cells operating consistently at higher temperatures experience accelerated ageing, reflected by negative SOH deviations (blue), while cells at lower temperatures show positive deviations (red).

Supplementary Figure 11

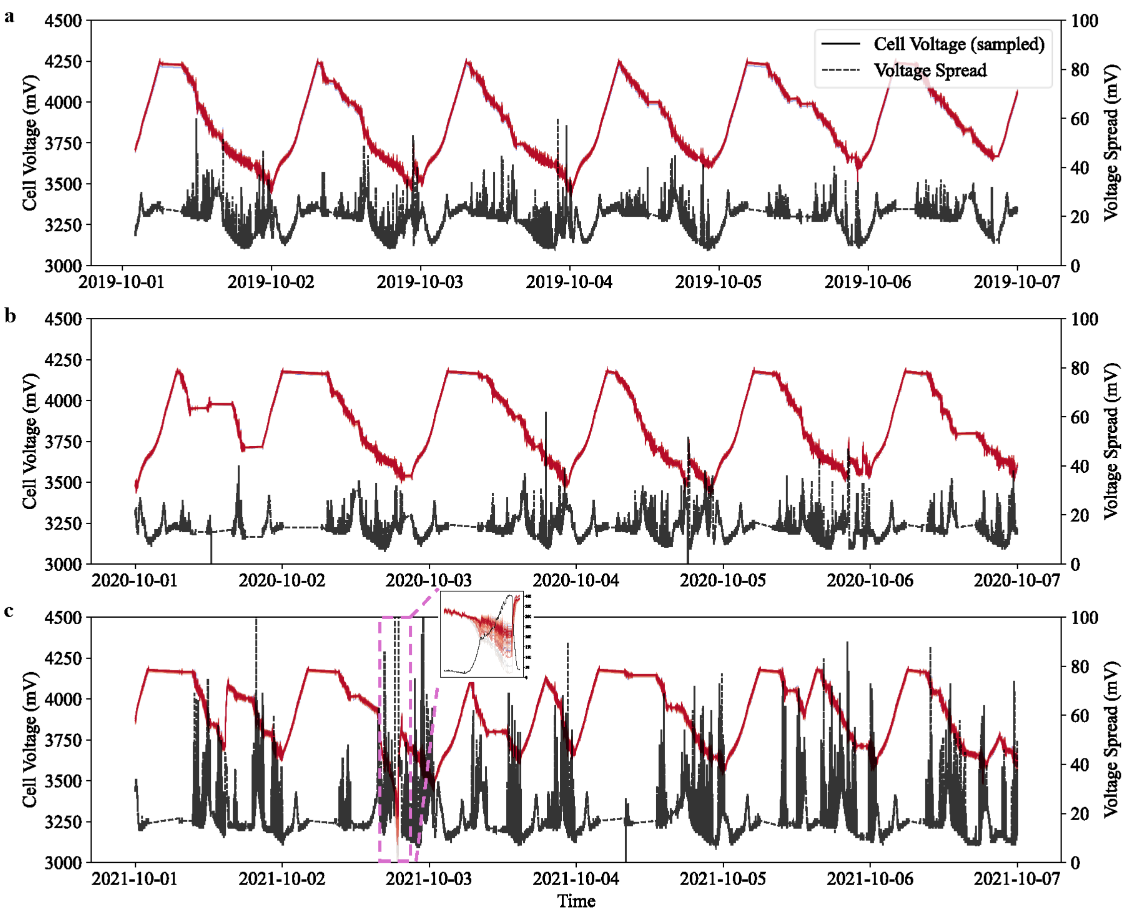

Supplementary Figure 11 | Evolution of cell voltage and voltage spread in the NMC battery pack of a passenger car across three observation windows. a, 1–7 October 2019. **b**, 1–7 October 2020. **c**, 1–7 October 2021. Red lines show sampled cell voltages (left axis) and black dashed lines indicate the corresponding voltage spread, defined as the maximum minus minimum cell voltage within the pack (right axis). The comparison across years highlights the effectiveness of continuous passive balancing in suppressing cell-to-cell divergence, with voltage spread remaining generally below 50 mV during early operation and rarely exceeding 100 mV even at later ageing stages.

Supplementary Figure 12

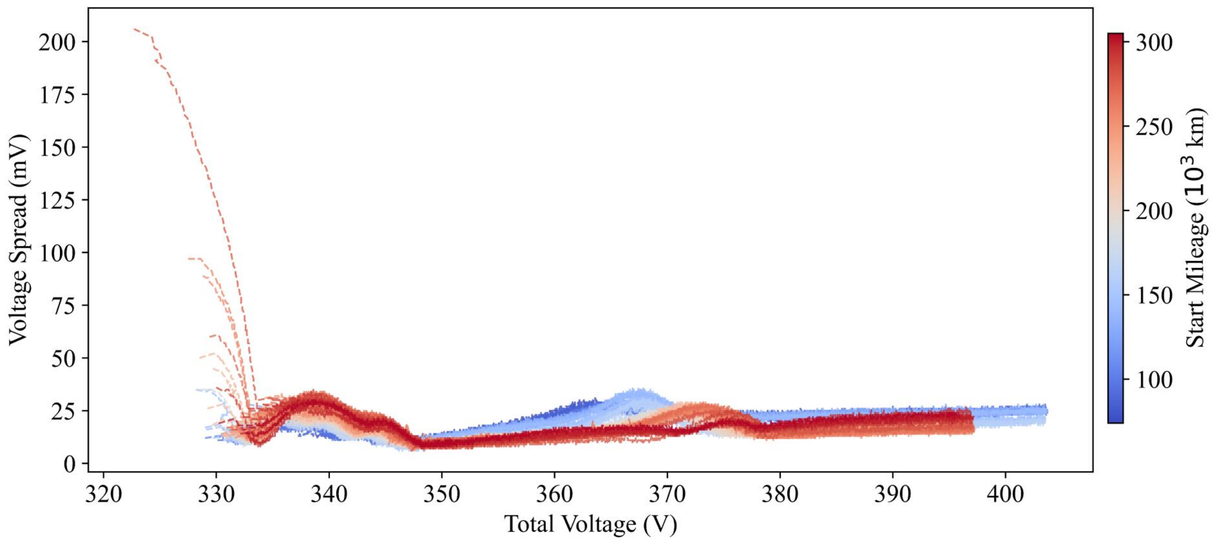

Supplementary Figure 12 | Evolution of voltage spread as a function of pack voltage in a representative NMC battery pack. The pack has a nominal capacity of 150 Ah and is charged to the 100% SOC at a low and constant current of 18 A.

Supplementary Figure 13

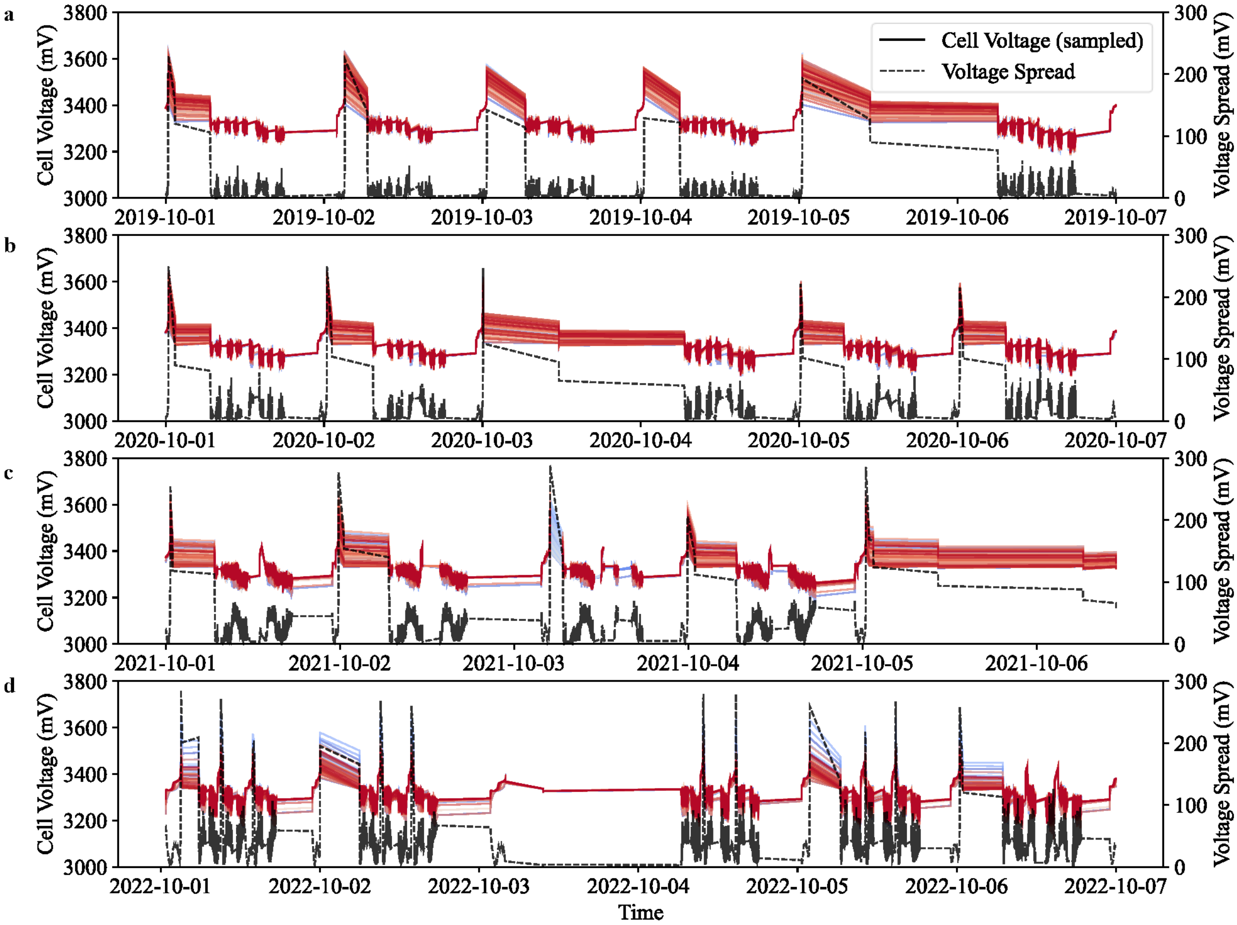

Supplementary Figure 13 | Evolution of cell voltage and voltage spread in an LFP bus battery pack across four observation windows. a, 1–7 October 2019. **b**, 1–7 October 2020. **c**, 1–7 October 2021. **d**, 1–7 October 2022. Red solid lines represent sampled cell voltages (left axis), and black dashed lines show the corresponding voltage spread, defined as the difference between maximum and minimum cell voltages within the pack (right axis). The comparison across years reveals a continuous increase in voltage spread, reaching nearly 300 mV at later ageing stages. This pronounced divergence underscores the absence of balancing in the LFP battery systems and highlights the necessity of effective balancing strategies to maintain pack uniformity.

Supplementary Figure 14

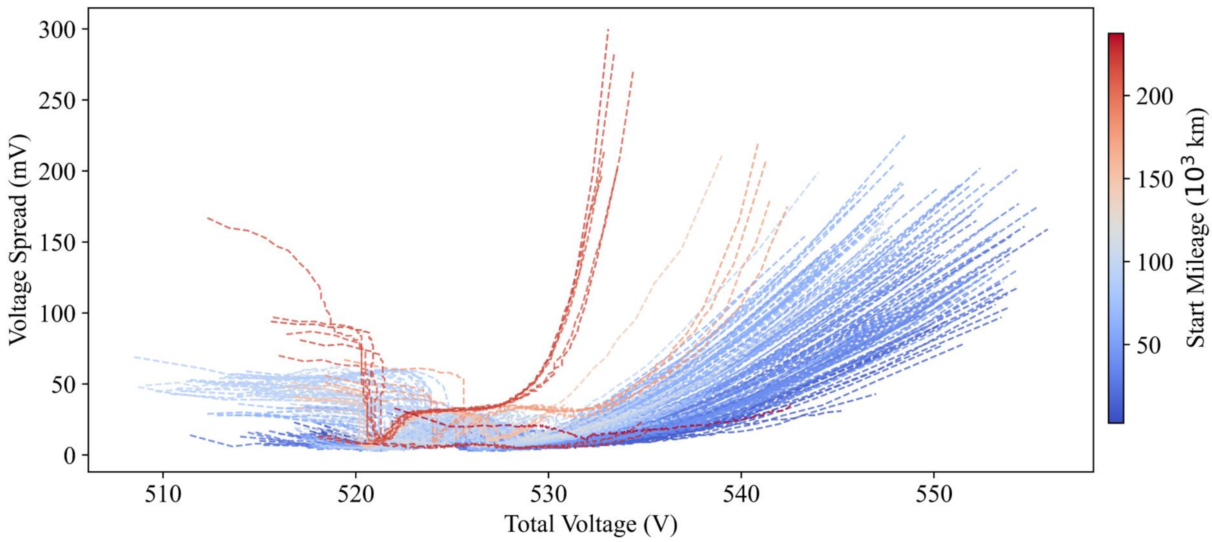

Supplementary Figure 14 | Evolution of voltage spread as a function of pack voltage in a representative LFP battery pack. The pack has a nominal capacity of 210 Ah and is charged to the 100% SOC at a low and constant current of 79 A.

Supplementary Figure 15

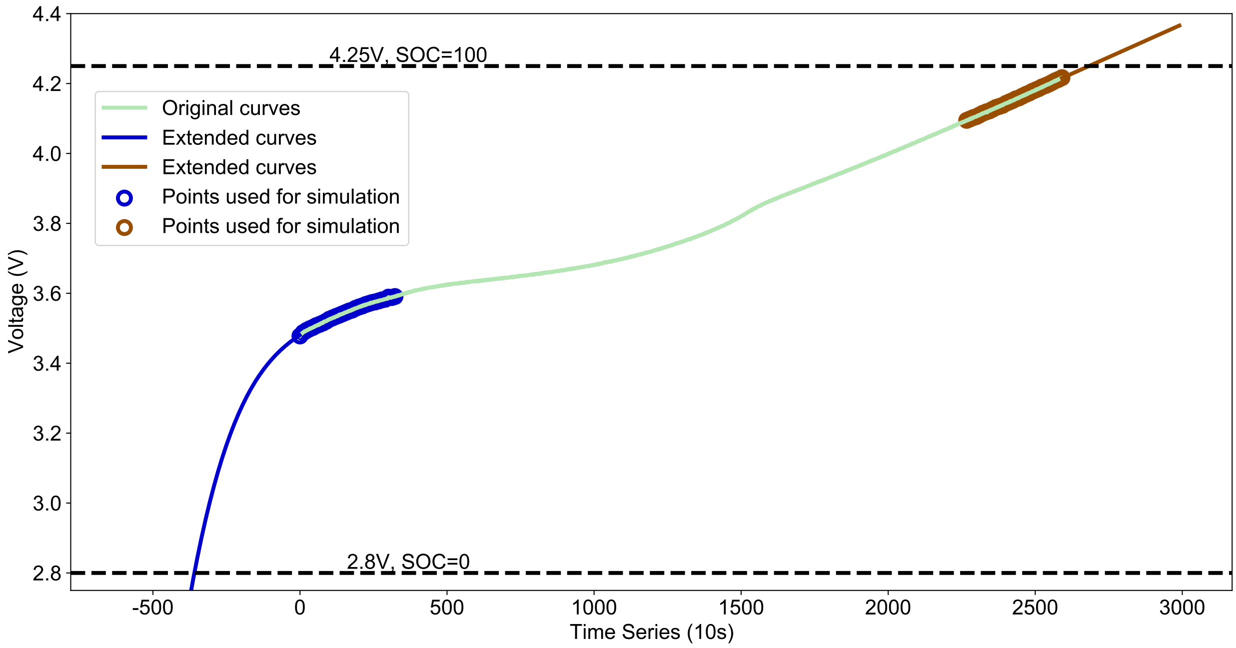

Supplementary Figure 15 | Illustration of the open-circuit voltage (OCV)–SOC curve for a lithium-ion battery cell. The green segment represents the partial OCV–SOC profile obtained from direct measurements. Blue and brown curves indicate extrapolated profiles at the low and high ends of the SOC range, respectively, based on transitional anchor points marked by blue and brown circles.

Supplementary Figure 16

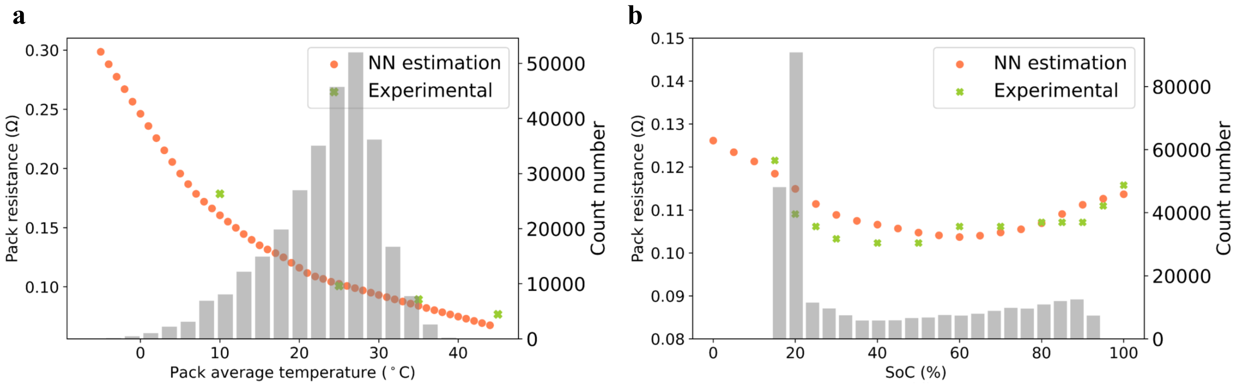

Supplementary Figure 16 | Validation of the estimation method on EV batteries at the beginning of life. a, Dependence of pack resistance on pack-average temperature, comparing neural-network (NN) estimations with experimental BoL measurements. The accompanying histogram indicates the number of field data points within each temperature interval. **b**, Dependence of pack resistance on SOC, with NN estimations and experimental results shown together. The histogram represents the distribution of field data across different SOC intervals.

Supplementary Figure 17

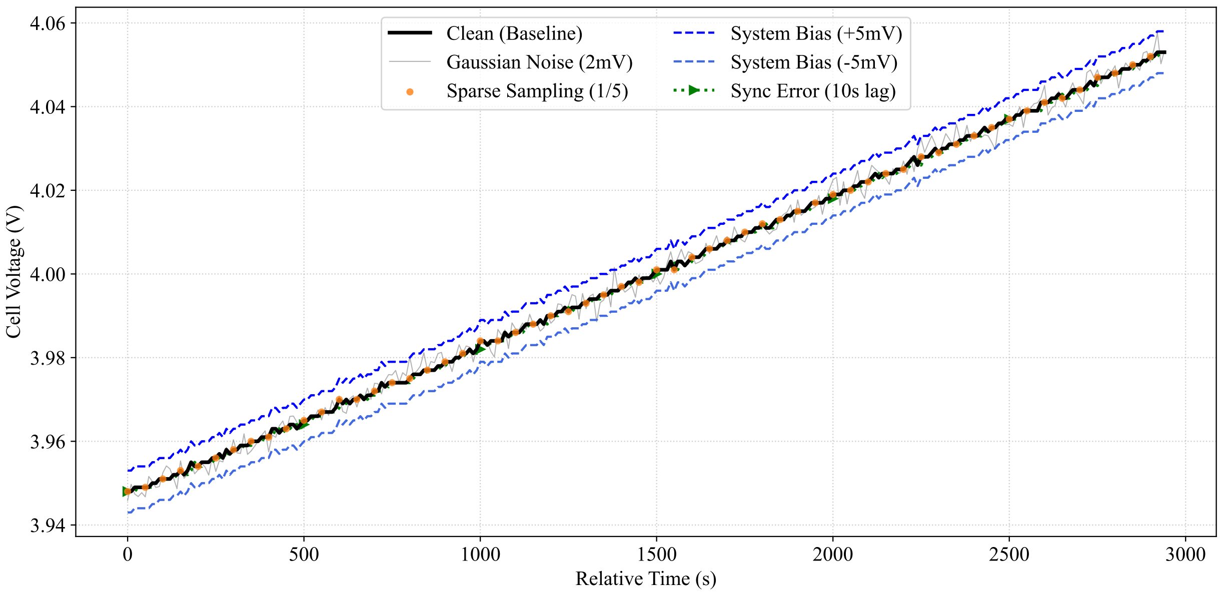

Supplementary Figure 17 | Terminal voltage signals under additional measurement perturbations. A representative segment of terminal voltage profiles from a randomly selected cell in the EV fleet dataset is shown for illustration. The baseline corresponds to the original fleet measurements, and four representative sensing perturbations are additionally introduced for robustness evaluation: additive Gaussian noise (σ = 2 mV), sparse sampling (retaining one out of five samples), systematic voltage bias (±5 mV), and synchronization error (10 s temporal lag).

Supplementary Figure 18

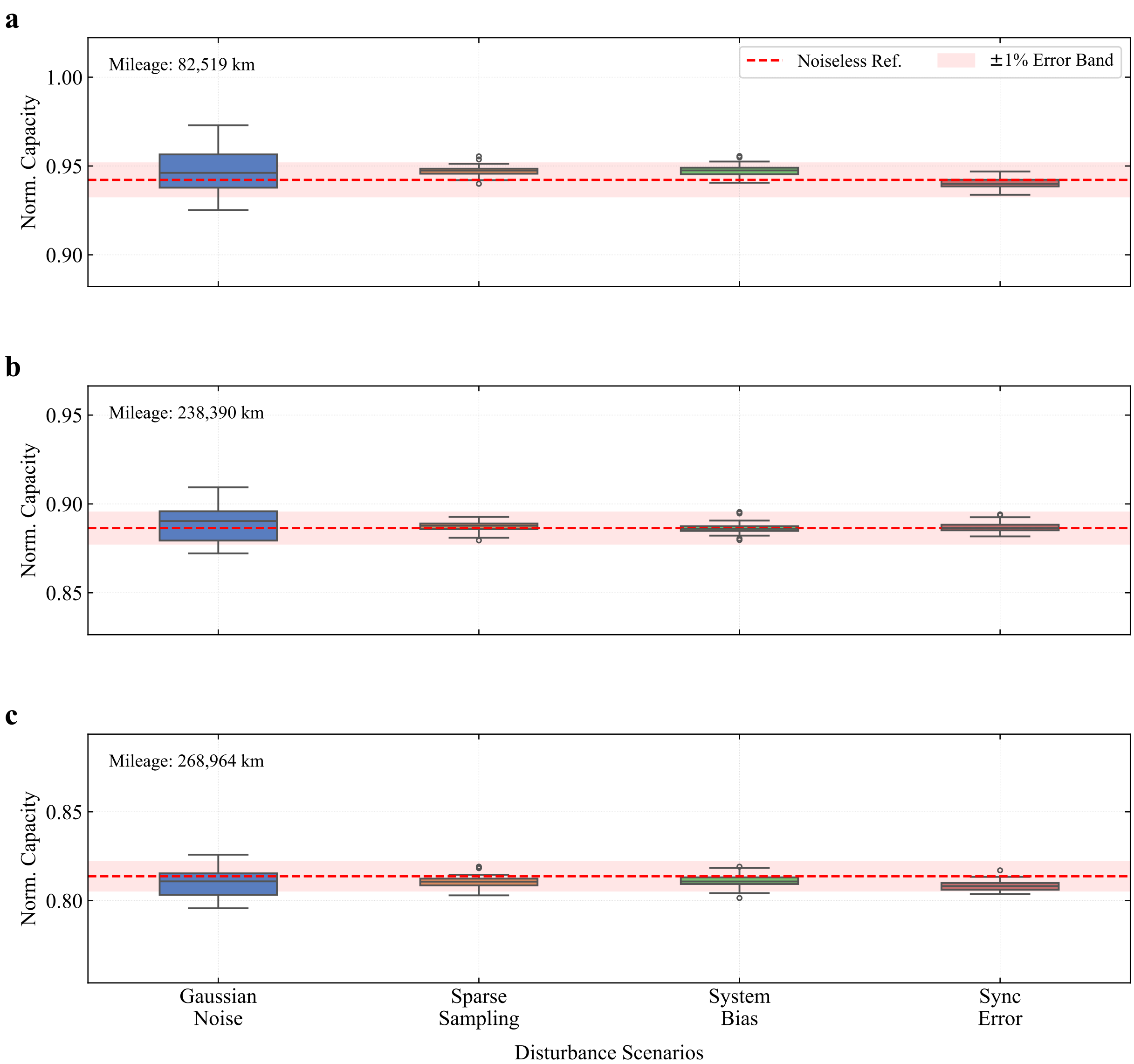

Supplementary Figure 18 | Robustness of capacity identification under measurement perturbations. Distribution of normalised cell capacity estimates obtained under four disturbance scenarios (Gaussian noise, sparse sampling, systematic voltage bias, and synchronization error) introduced to the fleet voltage measurements. Results are shown for three representative mileage levels (82,519 km, 238,390 km, and 268,964 km) from a vehicle in the EV fleet dataset. Each boxplot summarises 100 Monte Carlo identification trials. The red dashed line indicates the capacity estimate obtained from the baseline identification using the original fleet measurements (without additional perturbations), and the shaded region denotes the ±1% deviation band. For each box plot, the centre line indicates the median, box bounds indicate the 25th and 75th percentiles, whiskers extend to the most extreme non-outlier values within 1.5 times the interquartile range, and circles denote outliers.

Supplementary Figure 19

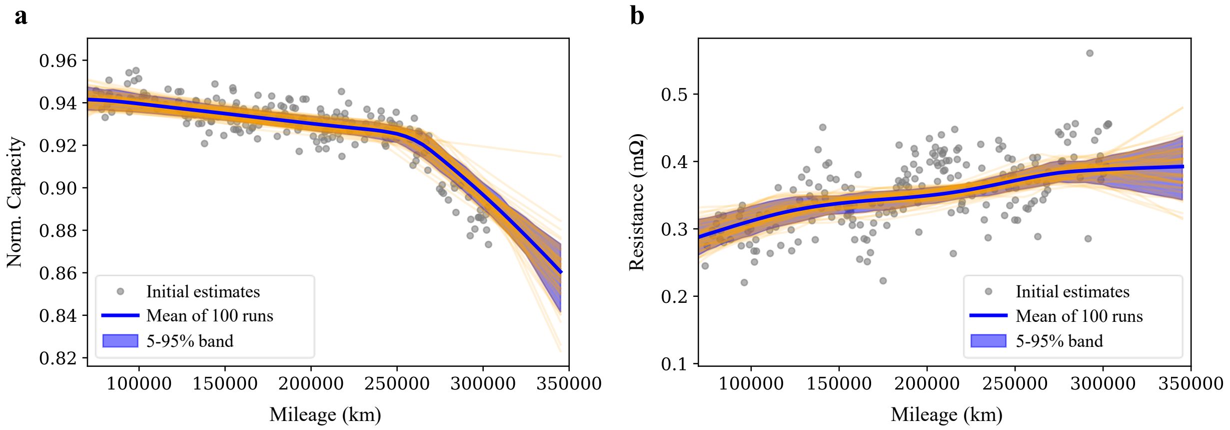

Supplementary Figure 19 | Sensitivity analysis of the proposed method in estimating capacity and resistance of a representative NMC cell. We trained the capacity (**a**) and resistance (**b**) neural-network models 100 times each with different random seeds, under both operational conditions and a standard reference condition. Grey dots represent ageing indicators estimated under varying ambient temperatures and operating conditions. Orange curves denote the normalised capacity or resistance values projected onto the reference condition for each run. The blue line shows the mean across all the 100 runs; the blue shaded band indicates a 5–95% confidence interval.

Supplementary Figure 20

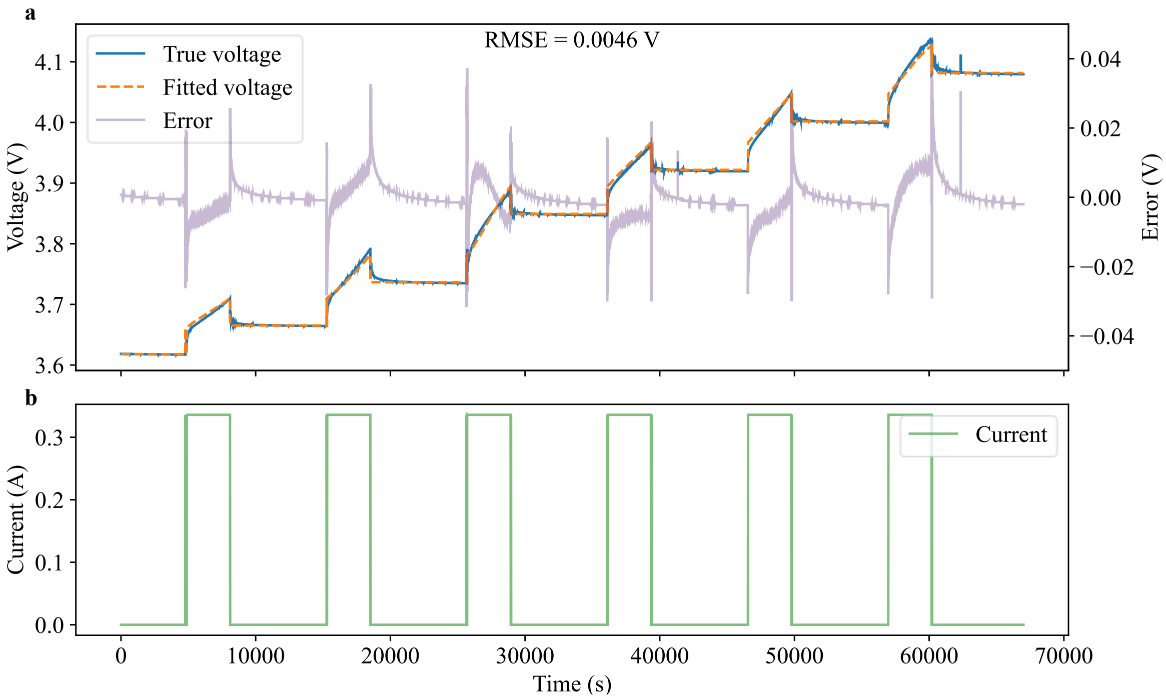

Supplementary Figure 20 | Validation of the parameter identification method under an HPPC test. a, Measured and model-predicted voltage responses, together with the residual trajectory. **b**, Applied HPPC current profile.

Supplementary Figure 21

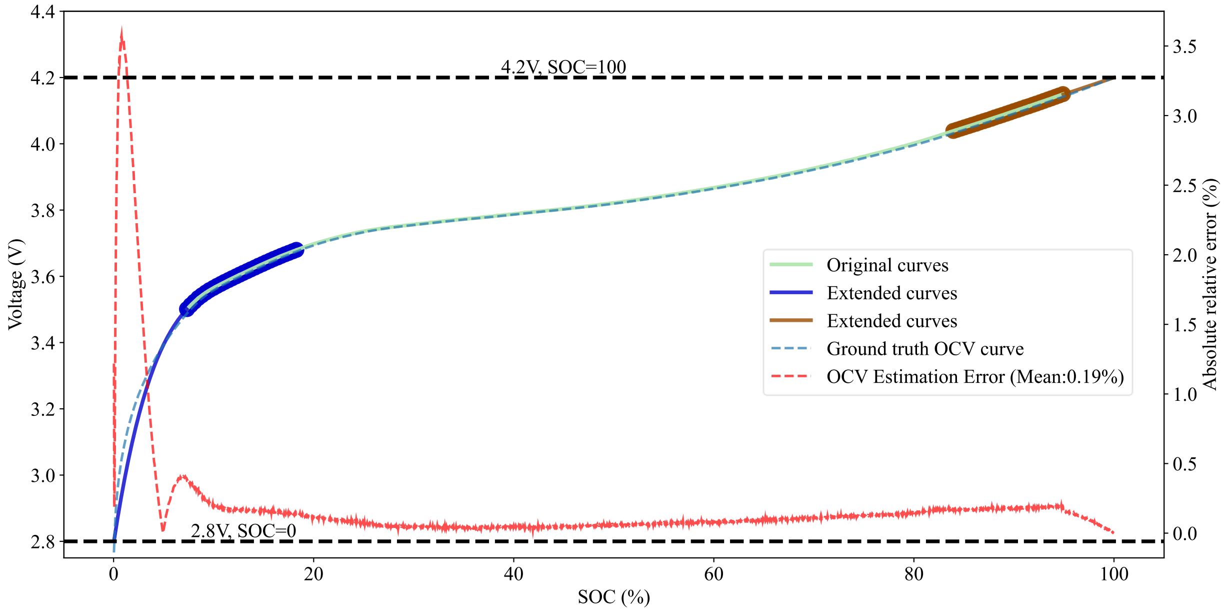

Supplementary Figure 21 | Validation of the estimated OCV curve on the Oxford dataset. The ground-truth OCV curve, calibrated under controlled laboratory conditions, covers the full SOC range and serves as the reference. The "Original curve" is the partial OCV–SOC profile obtained from direct measurements and transformation of terminal voltage data; here we assume only original curves of individual battery cells are available. The goal is to recover the blue and brown curves at the low and high SOC ends, respectively, using transitional points marked by blue and brown circles. The reconstructed OCV–SOC curve (solid lines) closely matches the ground-truth curve (dashed line), achieving a mean absolute relative error of 0.19 %. The estimation error (red dashed line, right axis) remains below 0.5 % for most of the SOC range, except at very low SOC values (< 5 %), which are rarely encountered in practice.

Supplementary Figure 22

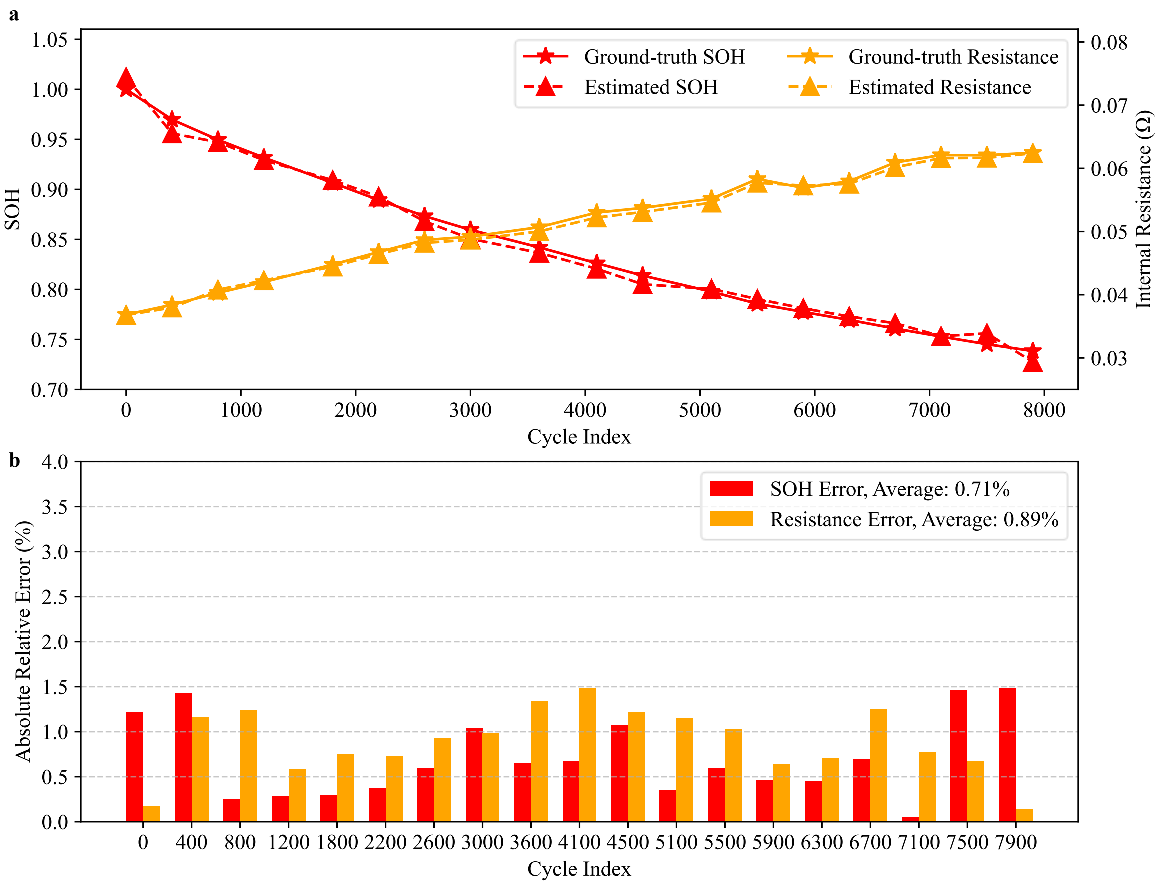

Supplementary Figure 22 | Validation of the estimation method using Oxford Battery Degradation Dataset 1. a, Comparison of the SOH and internal resistance between ground truth and estimated values. **b**, Mean absolute relative errors of the SOH and internal resistance.

Supplementary Figure 23

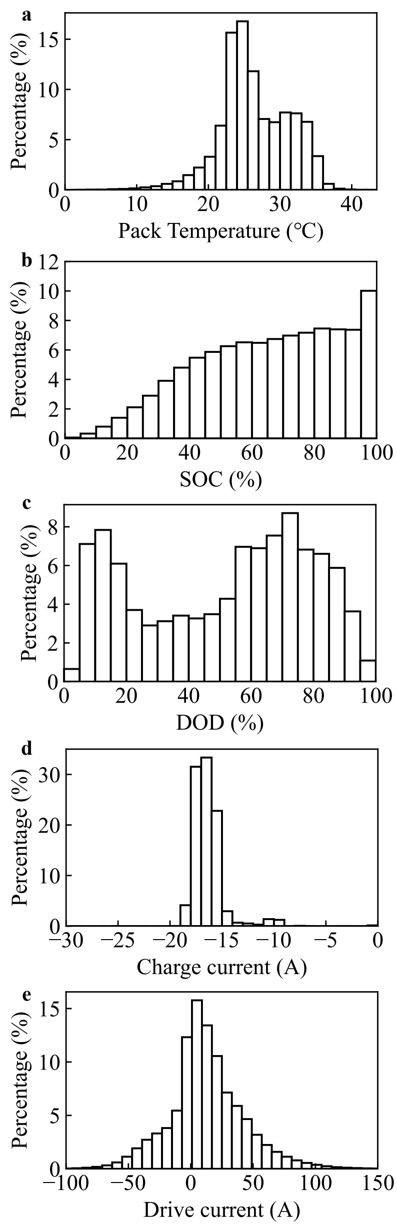

f

Pack Temperature	**Average**	**26.19**
	Variance	**23.14**
	Skewness	**0.19**
	Kurtosis	**0.32**
	Maximum	**43.00**
	Minimum	**1.00**

g

SOC	**Average**	**64.85**
	Variance	**532.50**
	Skewness	**0.32**
	Kurtosis	**-0.85**
	Maximum	**100.00**
	Minimum	**1.00**

h

DOD	**Average**	**51.34**
	Variance	**750.12**
	Skewness	**0.27**
	Kurtosis	**-1.27**
	Maximum	**98.00**
	Minimum	**3.00**

i

Charge Current	**Average**	**-17.41**
	Variance	**106.88**
	Skewness	**10.25**
	Kurtosis	**109.48**
	Maximum	**-0.20**
	Minimum	**-151.80**

j

Drive Current (>20km/h)	**Average**	**12.59**
	Variance	**921.50**
	Skewness	**0.39**
	Kurtosis	**1.74**
	Maximum	**333.60**
	Minimum	**-206.60**

Supplementary Figure 23 | Distributions of key stress factors for the NMC battery pack in a representative passenger car. a–e show the distributions of pack temperature, SOC, DOD, charging current, and driving current, respectively, for the selected car over the data collection period. **f**–**j** present the corresponding statistical properties of these stress factors.

Supplementary Figure 24

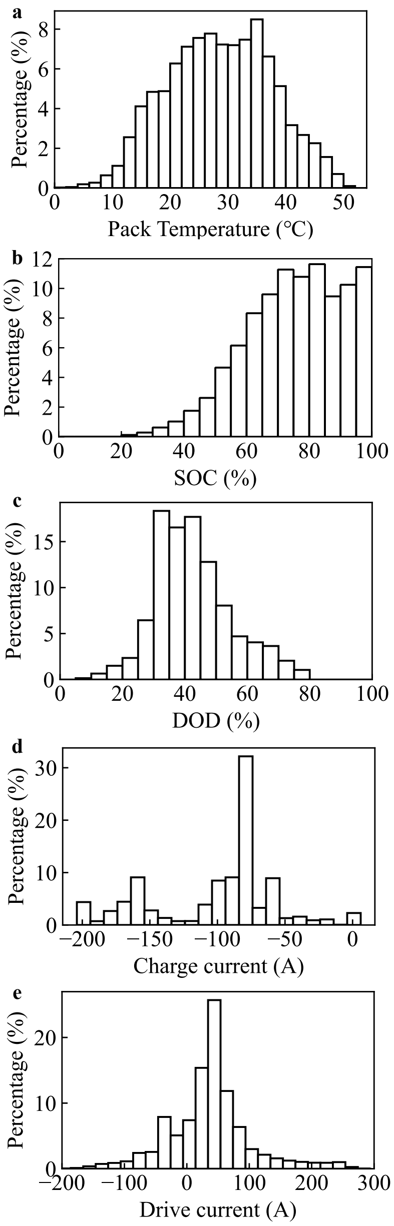

f

Pack Temperature	Average	28.22
	Variance	80.93
	Skewness	-0.03
	Kurtosis	-0.60
	Maximum	51.00
	Minimum	-1.00

g

SOC	Average	74.99
	Variance	249.39
	Skewness	-0.46
	Kurtosis	-0.33
	Maximum	100.00
	Minimum	19.00

h

DOD	Average	42.19
	Variance	153.73
	Skewness	0.53
	Kurtosis	0.23
	Maximum	78.00
	Minimum	8.00

i

Charge Current	Average	-100.12
	Variance	2054.14
	Skewness	-0.56
	Kurtosis	0.20
	Maximum	3.90
	Minimum	-203.7

j

Drive Current (>20km/h)	Average	36.31
	Variance	4303.91
	Skewness	0.38
	Kurtosis	1.76
	Maximum	283.50
	Minimum	-205.80

Supplementary Figure 24 | Distributions of key stress factors for the LFP battery pack in a representative bus. a–e show the distributions of pack temperature, SOC, DOD, charging current, and driving current, respectively, for the selected bus over the data collection period. **f–j** present the corresponding statistical properties of these stress factors.

Supplementary Figure 25

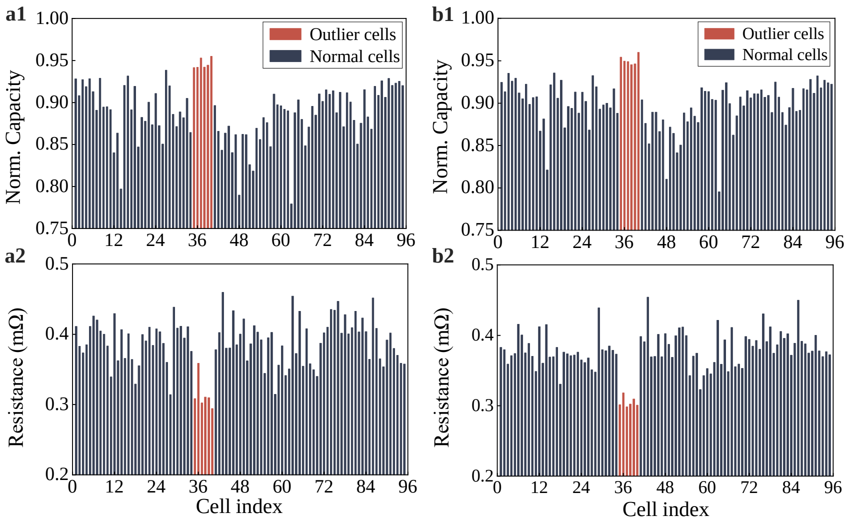

Supplementary Figure 25 | Normalised capacity and resistance of NMC battery cells in an electric car at an accumulated mileage of 287,838 km. a1 and **a2** show the estimates under operational conditions, while **b1** and **b2** present the estimates projected onto a reference condition. In this pack, several degraded cells were replaced with new ones (annotated as "Outlier cells") during service, leading to increased cell-to-cell dispersion. The clear detection of this maintenance-related shift by our method demonstrates its ability to capture both natural ageing effects and operational interventions.

Supplementary Figure 26

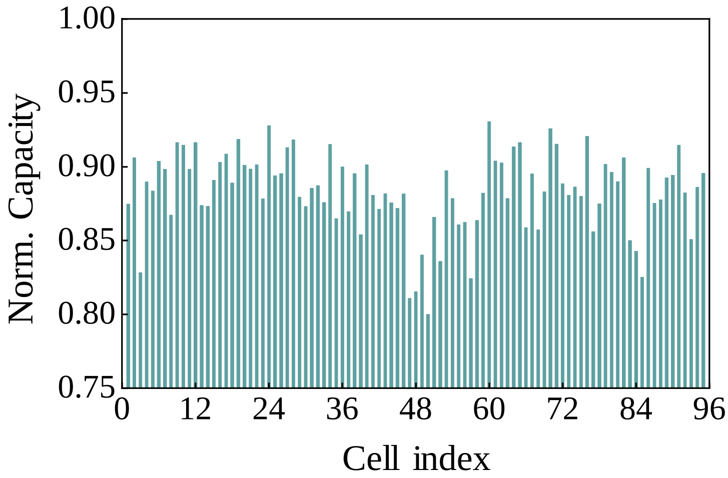

Supplementary Figure 26 | Distribution of normalised cell capacities in an NMC passenger car pack after 280,000 km. All 95 cell capacities are normalised to their nominal beginning-of-life value. The pack-level SOH is limited by the weakest cell with an SOH of 80%, while individual cell SOH values range from 80% to 93%.

Supplementary Figure 27

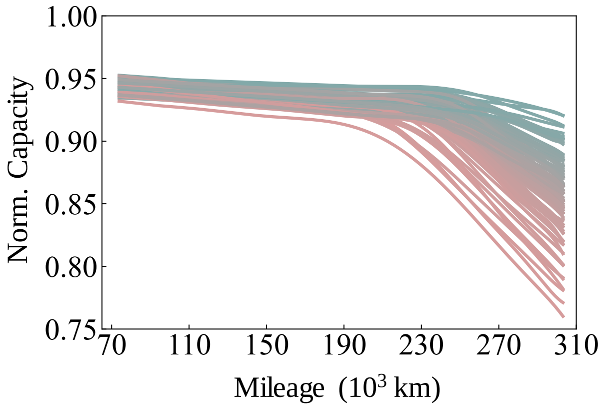

Supplementary Figure 27 | Ageing trajectories for all 95 NMC cells in the battery pack of an electric passenger car. Normalised capacity versus mileage for these cells illustrates initially tight dispersion followed by accelerated divergence with ageing.

Supplementary References

[1] F. von Bülow, F. Heinrich, W. A. Paxton, The future of battery data and the state of health of lithium-ion batteries in automotive applications, Commun. Eng. 3 (1) (2024) 173.

[2] D. Zhao, Z. Zhou, P. Zhang, Y. Zhang, Z. Feng, Y. Yang, Y. Cao, Health condition assessment of satellite Li-ion battery pack considering battery inconsistency and pack performance indicators, J. Energy Storage 60 (2023) 106604.

[3] Y. A. Sultan, A. A. Eladl, M. A. Hassan, S. A. Gamel, Enhancing electric vehicle battery lifespan: integrating active balancing and machine learning for precise RUL estimation, Sci. Rep. 15 (1) (2025) 777.

[4] Z. Wei, H. Cui, X. Liu, Y. Li, R. Wang, Real-time reconfiguration-based all-cell flexibility and capacity maximum utilization of second-life batteries, IEEE Trans. Transport. Electrif. 11 (1) (2024) 1035–1047.

[5] D. F. Frost, D. A. Howey, Completely decentralized active balancing battery management system, IEEE Trans. Power Electron. 33 (1) (2017) 729–738.

[6] V. Azimi, A. Allam, S. Onori, Extending life of lithium-ion battery systems by embracing heterogeneities via an optimal control-based active balancing strategy, IEEE Trans. Contr. Syst. Technol. 31 (3) (2023) 1235–1249.

[7] W. Han, T. Wik, A. Kersten, G. Dong, C. Zou, Next-generation battery management systems: Dynamic reconfiguration, IEEE Ind. Electron. Mag. 14 (4) (2020) 20–31.

[8] Q. Ouyang, A. Škegro, L. Hu, W. Han, D. Ren, C. Geng, T. Wik, C. Zou, Mathematical modeling for reconfigurable battery systems with parallel–series connections, IEEE Trans. Control Syst. Technol. 34 (1) (2026) 186–202.

[9] Y. Weng, C. Ababei, AI-assisted reconfiguration of battery packs for cell balancing to extend driving runtime, J. Energy Storage 84 (2024) 110853.

[10] Y. Zhang, Data-driven battery aging diagnostics and lifetime extension, Ph.D. thesis, Chalmers University of Technology (2024). URL `https://research.chalmers.se/en/publication/543724`

[11] C. Birkl, Diagnosis and prognosis of degradation in lithium-ion batteries, Ph.D. thesis, University of Oxford (2017).

[12] D. Howey, C. Birkl, Oxford battery degradation dataset 1, University of Oxford. Dataset. https://ora.ox.ac.uk/objects/uuid:03ba4b01-cfed-46d3-9b1a-7d4a7bdf6fac, accessed: 2025-08-21 (2017).